AGU PUBLICATIONS

Geophysical Research Letters

RESEARCH LETTER
10.1002/2017GL076148

Key Points:
- The 17 July 2017 Komandorsky Islands earthquake ruptured the back-arc Bering Fracture Zone between the Komandorsky Sliver and Bering Plate
- Right-lateral strike-slip faulting with patchy slip extended ~400 km along strike including a southeastern large-slip patch ~100 km long
- The slip was sufficient to release strain accumulated since the last rupture in 1858; the BFZ is the primary plate boundary in the region

Supporting Information:
- Supporting Information S1
- Movie S1

Correspondence to:
T. Lay,
tlay@ucsc.edu

Citation:
Lay, T., Ye, L., Bai, Y., Cheung, K. F., Kanamori, H., Freymueller, J., … Kogan, M. G. (2017). Rupture along 400 km of the Bering fracture zone in the Komandorsky Islands earthquake (M_W 7.8) of 17 July 2017. *Geophysical Research Letters*, *44*. https://doi.org/10.1002/2017GL076148

Received 23 OCT 2017
Accepted 1 DEC 2017
Accepted article online 8 DEC 2017

Rupture Along 400 km of the Bering Fracture Zone in the Komandorsky Islands Earthquake (M_W 7.8) of 17 July 2017

Thorne Lay[1], Lingling Ye[2], Yefei Bai[3], Kwok Fai Cheung[3], Hiroo Kanamori[2], Jeffrey Freymueller[4], Grigory M. Steblov[5,6], and Mikhail G. Kogan[7]

[1]Department of Earth and Planetary Sciences, University of California, Santa Cruz, CA, USA, [2]Seismological Laboratory, California Institute of Technology, Pasadena, CA, USA, [3]Department of Ocean and Resources Engineering, University of Hawai'i at Manoa, Honolulu, HI, USA, [4]Geophysical Institute, University of Alaska Fairbanks, Fairbanks, AK, USA, [5]Schmidt Institute of Physics of the Earth, Russian Academy of Sciences, Moscow, Russia, [6]Geophysical Survey, Russian Academy of Sciences, Obninsk, Russia, [7]Lamont-Doherty Earth Observatory, Columbia University, New York, NY, USA

Abstract The 17 July 2017 Komandorsky Islands M_W 7.8 earthquake involved arc-parallel right-lateral patchy strike-slip faulting along ~400 km of the Bering Fracture Zone (BFZ) in the westernmost Aleutian Islands back arc. The large size of the earthquake indicates that the BFZ serves regionally as the primary plate boundary extending from the Near Islands to Kamchatka, with the fore-arc Komandorsky Sliver translating rapidly parallel to the Aleutian Trench. The slip distribution is determined by analysis of seismic, tsunami, and geodetic observations. Fault displacements of 4 to 8.5 m, mostly in the upper 15 km, but with localized extension to 20 to 30 km depth along a ~100 km long segment of the BFZ, are comparable to the possible slip deficit since the last major earthquakes in this region in 1849 and 1858, given an estimated 5.1 cm/yr rate between the Komandorsky Sliver and the Bering Plate.

Plain Language Summary A large earthquake struck the westernmost portion of the Aleutian Island arc on 17 July 2017. In this region the Pacific plate is moving relative to the North American plate parallel to the plate boundary, with no convergence. As a result the plate motion is accommodated on a strike-slip fault in the upper plate, located along the Bering Fracture Zone. The earthquake produced slip and aftershocks along a 400 km long stretch of the Bering Fracture Zone in a magnitude 7.8 earthquake. The slip distribution and time history are determined by modeling seismic, geodetic, and tsunami data. The event is comparable in length and seismic moment to the 1906 San Francisco earthquake on the San Andreas Fault.

1. Introduction

The westernmost Aleutians is one of the few subduction zone sections for which relative plate motions increase in obliquity all the way to trench-parallel shearing, with a cessation of convergence (Figure 1a). Slip partitioning progressively increases westward along the curved Aleutian arc (Avé Lallemant, 1996; Avé Lallemant & Oldow, 2000; Ekström & Engdahl, 1989), with the primary upper plate faulting migrating from fore-arc faults to the back-arc west of 172°E. Relative shearing motion between the Pacific Plate and North American Plate is ~7.8 cm/yr along this region (Figure 1a), with slip partitioning having activated back-arc strike-slip faulting along the Bering Fracture Zone (BFZ), resulting in the Komandorsky Sliver (KS). The BFZ formed during the spreading that began in the Komandorsky Basin west of the Shirshov aseismic ridge around 25 Ma (e.g., Yogodzinski et al., 1993).

Recent GPS measurements indicate motion of the KS almost parallel to the Pacific Plate motion (Figure 1b), at 5.1 cm/yr, about two thirds of the Pacific-North America rate (Kogan et al., 2017). Paleomagnetic observations (Minyuk & Stone, 2009) of the Komandorsky Islands (Bering and Medny) indicate localized internal clockwise rotation within the KS. The upper plate in this region is the Bering Plate (or Bering Block) (e.g., Cross & Freymueller, 2008; Lander et al., 1994; Mackey et al., 1997), which has minor clockwise rotation relative to North America, so the Pacific-Bering relative motion is almost the same as the Pacific-North America motion. The BFZ is thus proposed to be the primary tectonic plate boundary in the westernmost Aleutians (Figure 1), with right-lateral strike-slip faulting (Kogan et al., 2017). About 2.7 cm/yr of relative motion between the Pacific Plate and the KS is accommodated either by strike-slip faulting on the shallow-dipping megathrust or by deformation on fore-arc faults (Geist & Scholl, 1994).

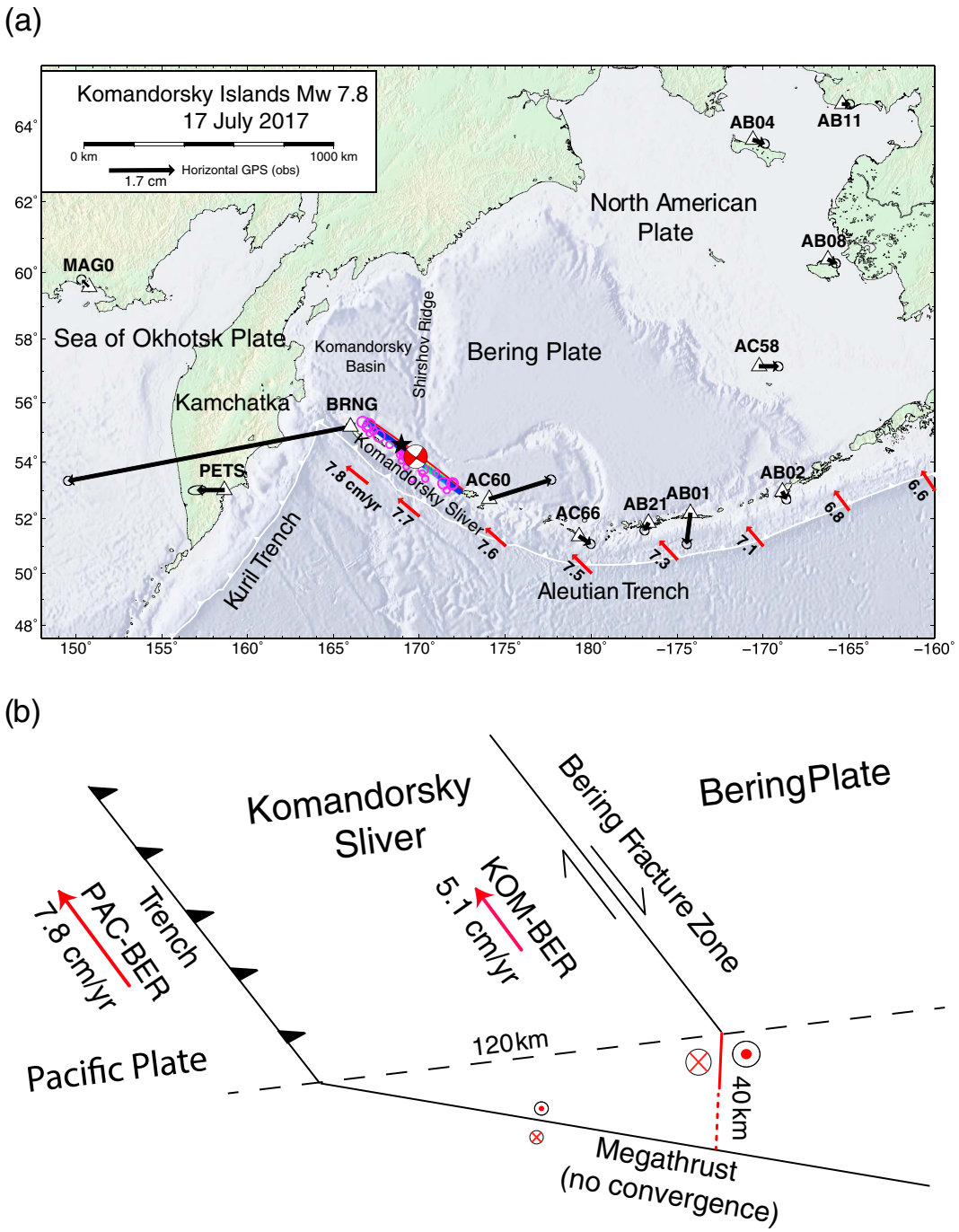

Figure 1. (a) Map showing location of the 17 July 2017 Komandorsky Islands earthquake hypocenter (star), the right-lateral strike-slip *W*-phase faulting mechanism, and first day aftershocks (magenta circles) in the westernmost Aleutians, along with GPS horizontal deformation on that day (black arrows) and motion of the Pacific Plate relative to the North American Plate for model MORVEL (red arrows). The earthquake occurred on the Bering fracture zone, which accommodates motion between the Komandorsky Sliver and the Bering Plate, as the sliver translates with the Pacific Plate toward Kamchatka. (b) Schematic of the motion of the Komandorsky Sliver. Arrows show motion relative to the Bering Plate. The shallow dipping megathrust boundary experiences horizontal strike-slip faulting.

A major strike-slip earthquake with m_b 6.8 and M_S 7.7 (Figure S1 in the supporting information) struck the BFZ on 17 July 2017 (United States Geological Survey/National Earthquake Information Center (USGS/NEIC) hypocenter: 54.443°N 168.857°E, 10 km deep at 23:34:13.74 UTC: https://earthquake.usgs.gov/earthquakes/eventpage/us20009x42#executive). This is the largest well-recorded event to strike this region, and it provides an opportunity to assess the dominant tectonic faulting along the westernmost Aleutians. Eight shallow

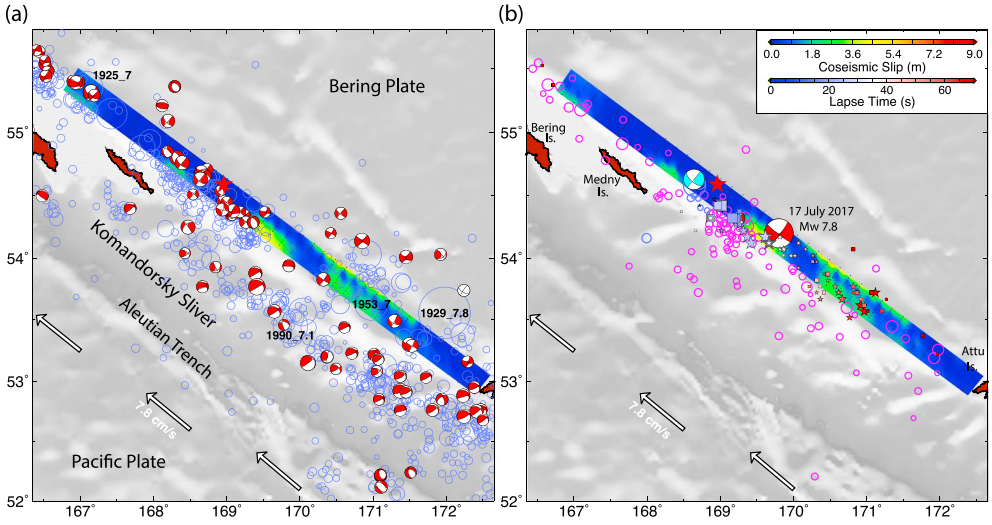

Figure 2. (a) Bilateral slip model for the 2017 earthquake and USGS/NEIC catalog seismicity from 1900 to 16 July 2017 (blue circles, scaled proportional to magnitude, with events larger than $M \sim 7$ being labeled), along with all moment tensor solutions from the GCMT catalog from 1976 to 16 July 2017 (red-filled compressional quadrant focal mechanisms). (b) Foreshock seismicity on 17 July 2017 (blue circles) and aftershock seismicity in the first 2 weeks (magenta circles) along with the M_W 6.3 foreshock GCMT focal mechanism (cyan focal mechanism). The large focal mechanism is the *W*-phase moment tensor from this study. The boxes indicate short-period radiators from the Eurasia-Greenland back projection, and stars indicate radiators from the North American back projection (Figure 3). The slip distribution is shown in detail in Figure S12. White vectors indicate the relative motion of the Pacific Plate to North America (almost identical to that relative to the Bering Plate). The large red star indicates the main shock epicenter.

foreshocks with $m_b \geq 4$ occurred within 12 h before the main shock near the hypocenter (Figure 2b), commencing with an M_W 6.3 strike-slip event (strike 130°, dip 68°, rake −179°). We invert long-period *W*-phase data (e.g., Kanamori & Rivera, 2008) from 99 global broadband stations using 235 channels, obtaining a main shock best double-couple solution with strike 127.9°, dip 84.4°, and rake −172.3°, and seismic moment $M_0 = 6.0 \times 10^{20}$ Nm (M_W 7.8). The centroid time shift was 45 s and the centroid location is 54.2°N, 169.8°E, 13.5 km deep, ~70 km southeast from the hypocenter (Figure 2b).

Figures 2a and S2 show seismicity from 1900 to the 2017 main shock from the USGS/NEIC catalog and all focal mechanisms from the Global Centroid Moment Tensor (GCMT) Catalog (http://www.globalcmt.org/CMTsearch.html). Historical large events struck the region in 1849 and 1858 (e.g., Sykes et al., 1981), so the region was designated as a seismic gap, and there have been three $M \sim 7$ events near the BFZ in the last century. A 1929 event with $M \sim 7.8$ is located to the southeast, close to the Near Islands (Figure 2a). This event has similar M_S observations to the 2017 earthquake (Figure S1). Right-lateral strike-slip faulting dominates along the BFZ, but seaward faulting is likely to involve horizontal strike-slip motion on the shallow dipping megathrust at depths from 26 to 40 km. The latter activity intensifies east of 170°E within the westernmost rupture area of the 1965 (M_W 8.7) Rat Island Earthquake. Along the KS there is no seismicity deeper than 50 km and no high seismic velocity aseismic slab material below 100 km (Levin et al., 2013). The northwestern end of the Aleutian trench involves underthrusting of the Pacific Plate beneath Kamchatka (Figure 1a) and collision of the KS with the Sea of Okhotsk plate (e.g., Cook, Fujita, & McMullen, 1986; Savostin, Verzhbitskaya, & Baranov, 1982).

We characterize the faulting in the 2017 Komandorsky Islands event, comparable in length and seismic moment to the 1906 San Francisco earthquake on the San Andreas Fault, using teleseismic, tsunami, and geodetic observations to evaluate its role in the complex tectonic environment of the westernmost Aleutians.

2. Data and Analysis Procedure

Kinematics of the 17 July 2017 earthquake are first assessed using back projection of short-period *P* waves from two large aperture seismic networks in North America and Eurasia to Greenland (Figure S3). Broadband signals are aligned using multistation correlation (Figures S4 and S5) and filtered to the passband 2.0 to 0.5 s, then back projected to the source region using the procedure of Xu et al. (2009). The results are summarized in Figure 3. The North America data suggest unilateral rupture with bursts of short-period

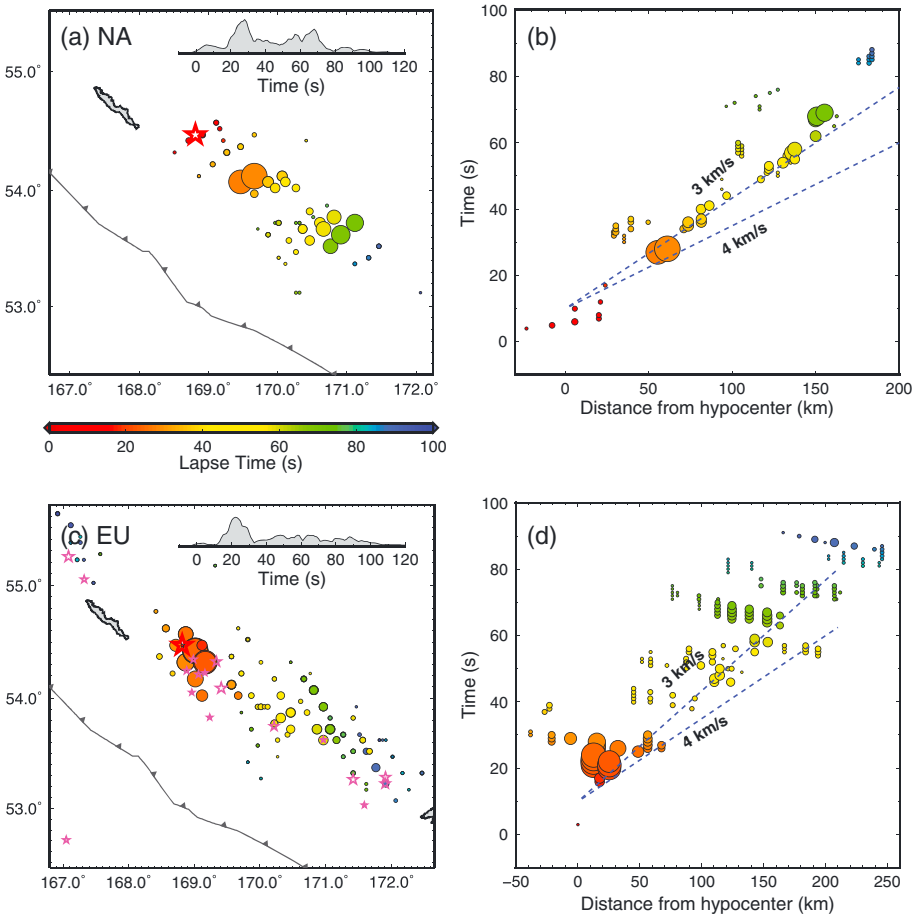

Figure 3. Back projection of short-period (2.0–0.5 s) *P* waves from large aperture networks of broadband stations in (a) North America and (c) Eurasia-Greenland. The station distributions and filtered signals are shown in Figures S3–S5. The position of peak stack amplitudes in 1 s time intervals are shown for the first 100 s after the origin time in the map views on the left and in the (b and d) corresponding linear distance-time plots. The large red star is the earthquake epicenter, magenta stars are large aftershocks within 24 h after the event. The time varying peak stack energy for each network is shown by insets in Figures 3a and 3c. The inferred rupture is largely unilateral along the arc toward the southeast, with ~3 km/s apparent rupture velocity following a delay of expansion of about 15 s.

radiation distributed along the fault strike over ~200 km, with two main concentrations ~50 and ~150 km southeast of the epicenter. The Eurasia image also features primarily southeastward expansion, but with minor bilateral radiation extending to northwest of Medny Island. The time-distance plots indicate very low short-period radiation in the first 15 s, followed by rupture expansion at ~3 km/s. Time-integrated images of the short-period energy beams are shown in Figure S6 and Movie S1 shows the time sequence.

Using faulting geometries guided by the *W*-phase solution and kinematic constraints from the back projections we invert for finite-fault rupture models using global teleseismic broadband *P* (86 stations) and *SH* (65 stations) ground displacements. Kinematic least squares inversions of the seismic waves based on Hartzell and Heaton (1983) and Kikuchi and Kanamori (1992) are performed. Model parameterization details are provided in Text S1. The seismic inversion results are used to forward model tsunami recordings and GPS displacements around the north Pacific, iteratively adjusting the kinematic inversion parameters to simultaneously fit the seismic, tsunami, and GPS observations (Figures 1, 4, 5, and S11).

We model signals from four northern Pacific deep-water ocean-bottom pressure sensor recordings at NOAA DART buoys (Figures 5 and S10). The steeply dipping strike-slip faulting of the 2017 event was not strongly tsunamigenic. The passage of surface waves generated strong oscillations in the DART signals that linger past the expected arrival of weak tsunami waves. Filtering the tide-corrected signals cannot remove the strong oscillations due to their high energy level and overlapping frequency band with the tsunami, precluding direct tsunami waveform inversion. Thus, we compare the recorded tsunami signals with predicted waveforms for different seismic models to bound poorly constrained model kinematic parameters. We calculate

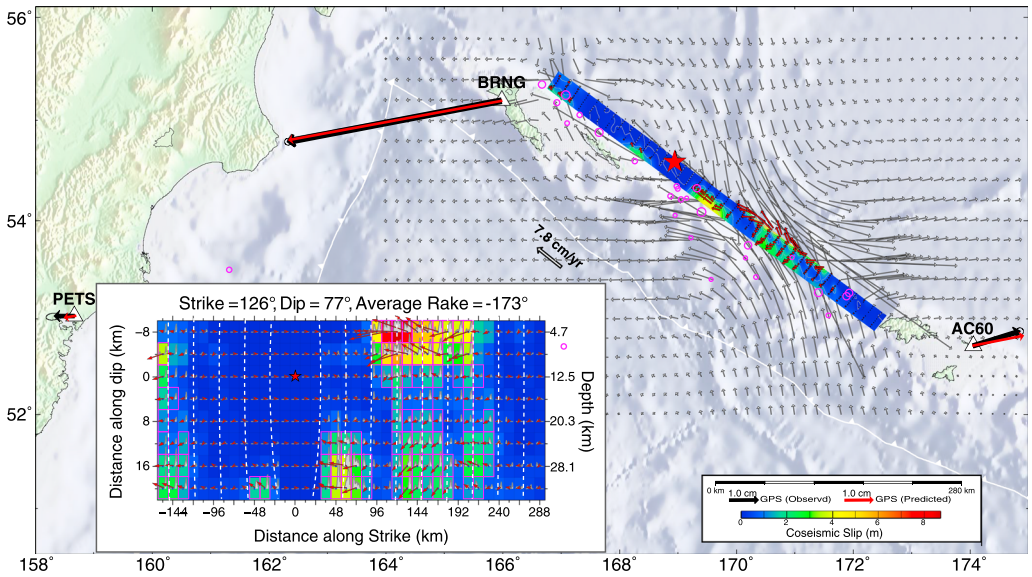

Figure 4. Comparison of observed (black arrows) and predicted (red arrows) GPS horizontal motions at stations BRNG, AC60, and PETS for the bilateral slip model. The length of the observed displacement vector at BRNG is 7.4 cm. The grid of slender vectors indicates the spatial variation of predicted horizontal surface motions on 1/20th scale. The bilateral slip model location is shown in the rectangle, with early aftershock locations indicated by magenta circles. The red star is the adjusted epicenter. The inset shows the slip distribution, as viewed from the southwest. Vectors indicate average slip and rake of the hanging wall (Komandorsky Sliver) relative to the footwall (Bering Plate). The color palette indicates the slip magnitude for each subfault. The subfault moment rate functions are shown by the polygons inside each slip, with total durations of up to 22 s. Isochrones of rupture front location in 10 s intervals are indicated by white dashes.

tsunami signals using the nonhydrostatic code NEOWAVE (Yamazaki, Kowalik, & Cheung, 2009, Yamazaki, Cheung, & Kowalik, 2011) for seafloor motions from the seismic kinematic rupture models. Iterative seismic inversion and tsunami forward modeling has been extensively applied to enhance resolution of offshore faulting, as the tsunami waveforms and timing provide valuable sensitivity to the faulting parameters (e.g., Bai et al., 2017; Heidarzadeh et al., 2016; Li et al., 2016; Yamazaki et al., 2011), including for deep water strike-slip faulting events (e.g., Gusman, Satake, & Harada, 2017). We model the northwest Pacific Ocean and Bering Sea at 1 arc min (1.85 km) resolution with the GEBCO bathymetry from British Oceanographic Data Center (Weatherall et al., 2015).

For determining GPS static deformations, we use solutions from the GAMIT/GLOBK software (Herring, King, & McClusky, 2010) for the sites in Russia and the GIPSY software for the sites in Alaska. Details of the processing are given in Text S1. The offset at PBO station AC60 (Shemya) is estimated by both methods, with consistent results. Most of the distant GPS observations in Figure 1 are local effects or noise, so we focus on the two stations closest to the rupture, BRNG, on Bering Island (55.19°N, 165.98°E) and AC60, east of Attu (52.71°N, 174.08°E). Vertical motions are not significant, so only horizontal offsets are considered. BRNG and AC60 are separated by ~600 km, near opposite ends of the 2017 rupture. We choose to iteratively forward model rather than invert these data, because their inclusion in finite-fault inversions is ill-posed (small slip close to isolated stations dominates the fitting). We seek a seismic inversion model that predicts these GPS data well using Okada half-space calculations (Okada, 1985), recognizing that over large distances along strike, there could be unresolved changes in faulting geometry.

3. Source Process Results

We consider models with either unilateral rupture propagating from the hypocenter toward the southeast, as suggested by the back projections, or bilateral rupture also including northwestward propagation. The seismic data and tsunami data can be fit in either case, with lower misfit for the unilateral rupture to the southeast, but the GPS displacements require slip to the northwest of the hypocenter.

Our initial seismic wave inversion for a unilateral rupture favors about 50 km southeastward placement of the main slip, with the best overall fit to the teleseismic signals achieved for a strike of 128°, dip of 67°, and average rake of −172° for the rake-varying inversion. We explore models with steep dip toward the

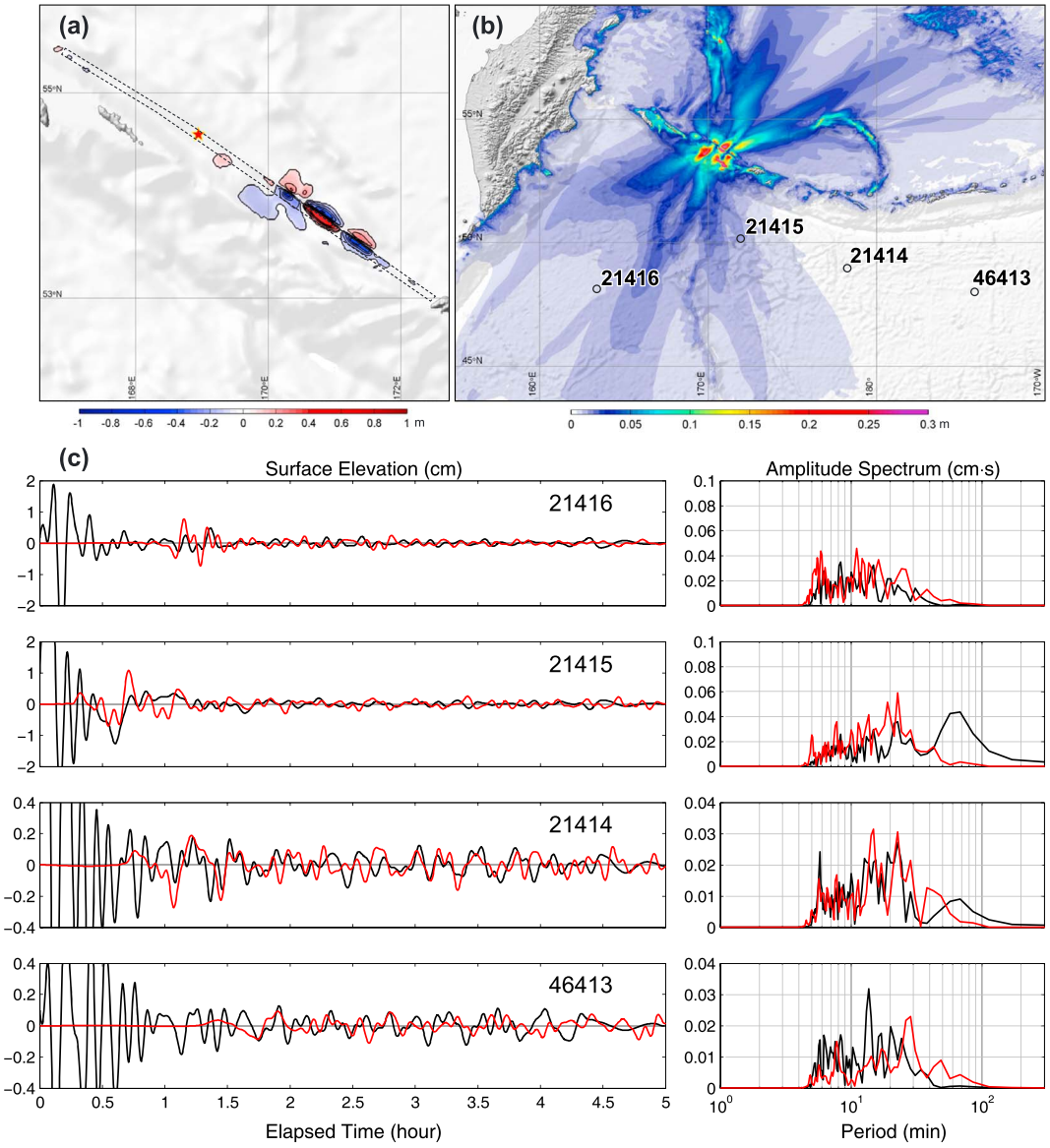

Figure 5. Predicted tsunami from the bilateral faulting model. (a) Final seafloor deformation with the red star indicating the epicenter and the dashed line delineating projection of the faulting model on the seafloor. (b) Predicted tsunami amplitude and DART stations (circles) considered in this study. (c) Comparison of filtered sea surface recordings (black) at DART stations with predictions (red) along with corresponding amplitude spectra (right). The recorded and predicted time series were filtered to remove signals shorter than 5 min period and the full 5 h time series were used in the computation of the amplitude spectra. The strike-slip faulting and position of the stations result in weak tsunami waves, but the timing and height of long-period arrivals provide bounds on the source.

northeast (for strike of 302°) as used in the USGS/NEIC finite-fault inversion, but the overall waveform fit is significantly degraded. The rather high waveform misfit is a consequence of the weak strike-slip radiation pattern for downgoing *P* and *SH* waves. The observed weak energy release in the first 15 s of the rupture raises the question of whether there was a distinct foreshock or an interval of rupture expansion with low seismic radiation. The teleseismic data do not tightly constrain the along-strike placement of slip, so we seek to improve resolution by modeling the tsunami signals and GPS data.

A suite of seismic finite-fault models inverted for rupture expansion velocities, *Vr*, ranging from 2.0 to 4.0 km/s and subfault source durations from 22 to 38 s, with dips varying from 62° to 77° for strike of 128° was used to predict tsunami observations for comparison with the four DART signals. The predicted tsunami arrival time and peak-to-trough height are compared to the recordings using subjective criteria (judging the agreement by eye), given the high noise level. The best-fitting unilateral model has a dip of 77°, $M_0 = 5.24 \times 10^{20}$ Nm (M_W 7.75), *Vr* = 2.15 km/s, and subfault duration of 22 s (Figures S7–S9). The *P* and *SH* data are well fit for this model

(Figure S8). The fit to the seismic data improves as the depth extent of the model increases, and this model has slip locally extending to 33 km depth. Predicted seafloor deformation (Figure S10) shows narrow strips of uplift and subsidence associated with the large near-surface shearing along the fault as well as a patch of subsidence from deeper slip of the rupture. The subsidence patch from the deeper slip produces a prominent leading trough in the side lobes to the east. The tsunami height at DART 21415 is well matched by the best unilateral model (despite the unstable baseline from the earlier seismic perturbations) and the long period signals at DART 21414 and 46413 are consistent with the data. The first tsunami amplitude at DART 21416 is overpredicted, but this is found for all of our models. However, this and other unilateral models severely underpredict the GPS displacement at BRNG and to a lesser extent the displacement at AC60 (Figure S11), as both stations are far from the slip zone.

Bilateral single-fault models with higher *Vr* and much longer fault length are required to match the displacement magnitude at BRNG and AC60. We consider planar fault models extending up to 500 km from along Bering Island to Attu, finding that minor slip near the stations can match the displacements. It is not likely that a single planar fault extends this far. We consider seismic inversion models for a range of strike from 120° to 128°, with rupture velocities from 2.0 to 4.0 km/s. Seismic inversion with $Vr = 3$ km/s places minor slip offshore of Bering island, matching the BRNG displacement magnitude, but not its direction, and the same is true for AC60, with both predictions being rotated clockwise. Shifting the hypocenter slightly, by 17 km at a bearing of 21° to 54.493°N, 168.957°E, allows good prediction of both GPS observations (Figure 4) for a seismic inversion using a planar fault model 468 km long. This model has patchy slip (Figures 4 and S12–S14), a centroid time of 57 s, and $M_0 = 6.17 \times 10^{20}$ Nm (M_W 7.79). It has a large slip patch to the southeast extending to 33 km depth, as in the unilateral model and a small slip patch at the northwestern end, off Bering Island, near some early aftershocks and historic activity (Figure 2). The resolution of depth of slip is very limited, and the GPS data can be fit well by models with slip constrained to the upper 15 km. Allowing deeper slip still provides the best overall fit, but this is dominated by the deeper slip in the large-slip patch far from the GPS stations. There is very little slip between the hypocenter and this slip patch off Bering Island, so it may well involve a distinct early aftershock, and the geometry need not be on a planar fault with rupture to the southeast. However, parsimoniously, it is possible to successfully predict the GPS data with a seismic inversion. The tsunami comparisons for this model (Figure 5) are slightly degraded from the unilateral model for station 21415 (Figure S10), but the overall waveforms are not incompatible, given the high noise level in the data. Thus, we present this as a preferred model that accounts for the seismic, GPS, and tsunami data well, with the caveat that a unilateral southeastward rupture with a northwestern early aftershock or aseismic slip near Bering Island is equally plausible. The minor hypocenter shift will trade-off with nonplanar faulting assumptions.

4. Fault Model Discussion and Conclusions

For the unilateral and bilateral models the total rupture duration is >80 s, with centroid times >54 s, exceeding the *W*-phase estimate due to the prolonged tail of the moment rate functions. In both cases, the initial strong slip occurs in a localized region near 30 km depth, rather than in the crust, and there is slip from 20 to ~30 km deep during the large southeastern crustal sliding. Given the rather young age of the seafloor in the Komandorsky Basin near the BFZ, this deep slip indicates that this was locally a lithospheric-transecting rupture on the primary plate boundary between the KS and the Bering Plate, but the resolution of slip depth is very limited northwest of the hypocenter and could all be less than 15 km deep.

The possibility that the deeper slip actually involved horizontal shearing on the underlying megathrust is considered, but two-fault models assuming such a geometry do not provide significant trench-parallel slip on a shallow-dipping plane. The depth of the megathrust is ~40 km below the seafloor at the BFZ, based on northwestward extrapolation from the Near Islands region of the slab contours for the Slab 1.0 model (Hayes, Wald, & Johnson, 2012), and using the 18° dip of the megathrust inferred by Kogan et al. (2017). We vary the depth from 25 to 40 km, but the megathrust radiation pattern is not favorable for accounting for the deep slip in our single-fault models.

We use the spectrum from the moment rate function for frequencies below 0.05 Hz, along with logarithmic stacking of propagation-corrected broadband *P* wave spectra to estimate the source spectra of the unilateral and bilateral models (Figures S9 and S14). The spectrum is deeply notched at around 0.02 Hz. For the two models, the estimates of broadband seismic radiated energy computed from the low-frequency moment

rate function and the average of individual station calculations for *P* waves are E_r = 1.98–2.18 × 10^{16} J for frequencies up to 1 Hz. The moment-scaled values are E_r/M_0 = 3.63–3.94 × 10^{-5}. The E_r/M_0 values are significantly higher than typical value of ~1.1 × 10^{-5} found for interplate thrust events (e.g., Ye et al., 2016). Static stress drop is computed using the procedures discussed by Ye et al. (2016), yielding slip-scaled stress drop estimates of 13.4 to 18 MPa (Figures S14 and S10). These are also high relative to most interplate thrust event results (~3–4 MPa).

Given that the last large events in the region were in 1849 and 1858, the potential slip deficit accumulated over the 160 year relative motion at an estimated rate of 5.1 cm/yr (Kogan et al., 2017) is about 8 m, so this event may have released all accumulated strain between the KS and the Bering Plate in the large slip patch. The 5.1 cm/yr rate was estimated for a uniform coupling depth of 12 km; the localized region of deeper slip in our preferred model could slightly increase that estimate, but the resolution of slip depth is too limited to improve the value. Little is known about the 28 September 1849 and 22 January 1858 events, as discussed by Sykes et al. (1981), but the 1849 event is thought to have generated a far-field tsunami so it seems unlikely to be a strike-slip event. The 1858 event is very poorly documented. Kondorskaya and Shebalin (1977) assign estimates of *M* 7.5 ± 0.7 to both events. Uncertainty in the mechanism, size, and slip location of these historic events limits our ability to evaluate whether the 2017 event is a recurrence event. However, the large size of the 2017 event, comparable to the 1906 San Francisco earthquake in both moment and length of rupture, establishes that the Bering Fracture Zone is serving as the likely primary plate boundary in the westernmost Aleutians, as proposed by Kogan et al. (2017).

Acknowledgments

The IRIS DMS data center (http://www.iris.edu/hq/) was used to access the seismic data from Global Seismic Network and Federation of Digital Seismic Network stations. Tsunami waveform data were obtained from the NOAA National Data Buoy Center (http://www.ndbc.noaa.gov/). Our GPS solutions are available from M. Kogan and J. Freymueller upon request. Raw data for all sites on the Alaska side are available from the UNAVCO archive, raw data for PETS are available from all IGS data centers, and raw data from BRNG are available from the Geophysical Survey of the Russian Academy of Sciences data center. We thank Kevin Furlong for discussions of the regional tectonics. Keith Koper shared his back projections of North American *P* waves, and Gavin Hayes shared his early finite-fault models with us. We appreciate comments and suggestions from two anonymous reviewers. This work was supported by National Science Foundation grant EAR1245717 to Thorne Lay.

References

Avé Lallemant, H. G. (1996). Displacement partitioning and arc-parallel extension in the Aleutian volcanic island arc. *Tectonophysics*, *256*(1-4), 279–293. https://doi.org/10.1016/0040-1951(95)00171-9

Avé Lallemant, H. G., & Oldow, J. S. (2000). Active displacement partitioning and arc-parallel extension of the Aleutian volcanic arc based on Global Positioning System geodesy and kinematic analysis. *Geology*, *28*(8), 739–742. https://doi.org/10.1130/0091-7613(2000)28%3C739:ADPAAE%3E2.0.CO;2

Bai, Y., Lay, T., Cheung, K. F., & Ye, L. (2017). Two regions of seafloor deformation generated the tsunami for the 13 November 2016, Kaikoura, New Zealand earthquake. *Geophysical Research Letters*, *44*, 6597–6606. https://doi.org/10.1002/2017GL073717

Cook, D. B., Fujita, K., & McMullen, C. A. (1986). Present-day interactions in Northeast Asia: North American, Eurasian and Okhotsk plates. *Journal of Geodynamics*, *6*(1-4), 33–51. https://doi.org/10.1016/0264-3707(86)90031-1

Cross, R. S., & Freymueller, J. T. (2008). Evidence for and implications of a Bering plate based on geodetic measurements from the Aleutians and western Alaska. *Journal of Geophysical Research*, *113*, B07405. https://doi.org/10.1029/2007JB005136

Ekström, G., & Engdahl, E. R. (1989). Earthquake source parameters and stress distribution in the Adak Island region of the central Aleutian Islands, Alaska. *Journal of Geophysical Research*, *94*, 15,499–15,519. https://doi.org/10.1029/JB09riB11p15499

Geist, E. L., & Scholl, D. W. (1994). Large-scale deformation related to the collision of the Aleutian arc with Kamchatka. *Tectonics*, *13*, 538–560. https://doi.org/10.1029/94TC00428

Gusman, A. R., Satake, K., & Harada, T. (2017). Rupture process of the 2016 Wharton Basin strike-slip faulting earthquake estimated from joint inversion of teleseismic and tsunami wavefomrs. *Geophysical Research Letters*, *44*, 4082–4089. https://doi.org/10.1002/2017GL073611

Hartzell, S. H., & Heaton, T. H. (1983). Inversion of strong ground motion and teleseismic waveform data for the fault rupture history of the 1979 Imperial Valley, California, earthquake. *Bulletin of the Seismological Society of America*, *73*(6A), 1553–1583.

Hayes, G., Wald, D. J., & Johnson, R. L. (2012). Slab 1.0: A three-dimensional model of global subduction zone geometries. *Journal of Geophysical Research*, *117*, B01302. https://doi.org/10.1029/2011JB008524

Heidarzadeh, M., Murotani, S., Satake, K., Ishibe, T., & Gusman, A. R. (2016). Source model of the 16 September 2015 Illapel, Chile, M_W 8.4 earthquake based on teleseismic and tsunami data. *Geophysical Research Letters*, *43*, 643–650. https://doi.org/10.1002/2015GL067297

Herring, T. A., King, R. W., & McClusky, S. C. (2010). *Introduction to GAMIT/GLOBK, version 3.4*. Cambridge: Massachusetts Institute Of Technology.

Kanamori, H., & Rivera, L. (2008). Source inversion of *W* phase: Speeding up seismic tsunami warning. *Geophysical Journal International*, *175*(1), 222–238. https://doi.org/10.1111/j.1365-246X.2008

Kikuchi, M., & Kanamori, H. (1992). Inversion of complex body waves—III. *Bulletin of the Seismological Society of America*, *81*(6), 2335–2350.

Kogan, M. G., Frolov, D. I., Vasilenko, N. F., Freymueller, J. T., Steblov, G. M., Ekström, G., … Prytkov, A. S. (2017). Plate coupling and strain in the far western Aleutian arc modeled from GPS data. *Geophysical Research Letters*, *44*, 3176–3183. https://doi.org/10.1002/2017GL072735

Kondorskaya, N. V., & Shebalin, N. V. (Eds) (1977). *New catalog of strong earthquakes in the territory of the U.S.S.R* (pp. 347–433). Moscow, U.S.S.R.: Nauka.

Lander, A. V., Bukchin, B. G., Droznin, D. V., & Kiryushin, A. V. (1994). The tectonic environment and source parameters of the Khailino, Koryakiya earthquake of March 8, 1991: Does a Beringia plate exist? Geodynamics and earthquake forecast. In *Computational seismology* (Vol. 26, pp. 103–121). Moscow: Nauka. (in Russian)

Levin, V., Shapiro, N. M., Park, J., & Ritzwoller, M. H. (2013). Slab portal beneath the western Aleutians. *Geology*, *33*(4), 253–256. https://doi.org/10.1130/G20863.1

Li, L., Lay, T., Cheung, K. F., & Ye, L. (2016). Joint modeling of teleseismic and tsunami wave observations to constrain the 16 September 2015 Illapel, Chile, M_W 8.3 earthquake rupture process. *Geophysical Research Letters*, *43*, 4303–4312. https://doi.org/10.1002/2016GL068674

Mackey, K. G., Fujita, K., Gunbina, L. V., Kovalev, V. N., Imaev, V. S., Koz'min, B. M., & Imaeva, L. P. (1997). Seismicity of the Bering Strait region: Evidence for a Bering block. *Geological Society of America Bulletin*, *25*, 979–982.

Minyuk, P. S., & Stone, D. B. (2009). Paleomagnetic determination of paleolatitude and rotation of Bering Island (Komandorsky Islands) Russia: Comparison with rotations in the Aleutian Islands and Kamchatka. *Stephan Mueller Special Publication Series*, *4*, 329–348. https://doi.org/10.5194/smsps-4-329-2009

Okada, Y. (1985). Surface deformation due to shear and tensile faults in a half-space. *Bulletin of Seismological Society of America*, *75*(4), 1135–1154.

Savostin, L. A., Verzhbitskaya, A. I., & Baranov, B. V. (1982). Holocene plate tectonics of the sea of Okhotsk region. *Doklady Academy of Science, USSR, Earth Science Section*, *266*, 62–65.

Sykes, L. R., Kisslinger, J. B., House, L., Davies, J. N., & Jacob, K. H. (1981). Rupture zones and repeat times of great earthquakes along the Alaska-Aleutian arc, 1784–1980. In D. W. Simpson & P. G. Richards (Eds.), *Earthquake Prediction* (pp. 73–80). Washington, DC: American Geophysical Union. https://doi.org/10.1029/ME004p0073

Weatherall, P., Marks, K. M., Jakobsson, M., Schmitt, T., Tani, S., Arndt, J. E., … Wigley, R. (2015). A new digital bathymetric model of the world's oceans. *Earth and Space Science*, *2*(8), 331–345. https://doi.org/10.1002/2015EA000107

Xu, Y., Koper, K. D., Sufri, O., Zhu, L., & Hutko, A. R. (2009). Rupture imaging of the M_W 7.9 12 May 2008 Wenchuan earthquake from back projection of teleseismic *P* waves. *Geochemistry, Geophysics, Geosystems*, *10*, Q04006. https://doi.org/10.1029/2008GC002335

Yamazaki, Y., Cheung, K. F., & Kowalik, Z. (2011). Depth-integrated, non-hydrostatic model with grid nesting for tsunami generation, propagation, and run-up. *International Journal for Numerical Methods in Fluids*, *67*(12), 2081–2107. https://doi.org/10.1002/fld.2485

Yamazaki, Y., Kowalik, Z., & Cheung, K. F. (2009). Depth-integrated, non-hydrostatic model for wave breaking and run-up. *International Journal for Numerical Methods in Fluids*, *61*(5), 473–497. https://doi.org/10.1002/fld.1952

Yamazaki, Y., Lay, T., Cheung, K. F., Yue, H., & Kanamori, H. (2011). Modeling near-field tsunami observations to improve finite-fault slip models for the 11 March 2011 Tohoku earthquake. *Geophysical Research Letters*, *38,* L00G15. https://doi.org/10.1029/2011GL049130

Ye, L., Lay, T., Kanamori, H., & Rivera, L. (2016). Rupture characteristics of major and great ($M_W \geq 7$) megathrust earthquake from 1990–2015: 1. Moment scaling relationships. *Journal of Geophysical Research: Solid Earth*, *121*, 821–844. https://doi.org/10.1002/2015JB012426

Yogodzinski, G. M., Rubenstone, J. L., Kay, S. M., & Kay, R. W. (1993). Magmatic and tectonic development of the western Aleutians: An oceanic arc in a strike-slip setting. *Journal of Geophysical Research*, *98*, 11,807–11,834. https://doi.org/10.1029/93JB00714

Geophysical Research Letters

Supporting Information for

Rupture Along 400 km of the Bering Fracture Zone in the Komandorsky Islands Earthquake (M_W 7.8) of 17 July 2017

Thorne Lay[1], Lingling Ye[2], Yefei Bai[3], Kwok Fai Cheung[3], Hiroo Kanamori[2], Jeffrey Freymueller[4], Grigory M. Steblov[5,6], and Mikhail G. Kogan[7]

[1]Department of Earth and Planetary Sciences, University of California Santa Cruz, Santa Cruz, California, USA, [2]Seismological Laboratory, California Institute of Technology, Pasadena, California, USA, [3]Department of Ocean and Resources Engineering, University of Hawaii at Manoa, Honolulu, Hawaii, USA, [4]Geophysical Institute, University of Alaska Fairbanks, Fairbanks, Alaska, USA, [5]Schmidt Institute of Physics of the Earth RAS, Moscow, Russia, [6]Geophysical Survey RAS, Obninsk, Kaluga Region, Russia, [7]Lamont-Doherty Earth Observatory, Columbia University, New York, USA.

Correspondence to: Thorne Lay, tlay@ucsc.edu

Contents of this file

Additional Supporting information (Files uploaded separately).

Movie A1. Animation of the back-projections from North America and Europe.

Introduction

Data processing and rupture parameterization details are provided in Text S1, with Figures S1 to S14 providing supporting information about the seismicity, back-projection imaging, and finite-fault modeling.

Text S1

We estimated GPS displacements in the ITRF2008 reference frame from two separate solutions. There were no significant differences for the two overlapping stations, AC60 and PETS, so solutions were selected from one or the other.

The Geophysical Survey of the Russian Academy of Sciences data center is used to process the data of the Kamchatka GPS Network including BRNG (Bering Island) and PETS (Petropavlovsk). We use the GAMIT/GLOBK software in three steps (Herring et al. 2010): (1) 24-hour data spans of our stations are combined with 8 nearest sites of the International GNSS Service; (2) Regional daily solutions of step 1 are treated as quasi-observations and combined with global daily solutions available from Scripps Orbit and Permanent Array Center (SOPAC) or from MIT using a Kalman filter; (3) Combined daily solutions of step 2 are constrained with the reference frame ITRF2008 updated at MIT and transformed relative to the North American plate. This last transformation has little impact on the displacements because of the short time span considered (less than 3 weeks total). Static offsets are estimated from mean station positions for 9 days before and 9 days after the earthquake.

The University of Alaska Fairbanks processed the data from the remaining sites, all part of the Plate Boundary Observatory (PBO). We use the GIPSY software and the analysis procedures described in Fu & Freymueller (2012). Each individual station was processed in Precise Point Positioning (PPP) mode (Zumberge et al., 1997) using the JPL final orbits and clock products. Positions from all stations for a single day from a large area encompassing all of Alaska and including PETS (but not BRNG) are combined into a single daily loosely-constrained solution, which is then transformed into the ITRF2008 reference frame. Static offsets are estimated from mean station positions for 4 days before and 4 days after the earthquake.

For the kinematic rupture model, we assume continuous rupture from the onset, parameterizing relatively long-duration subfault ruptures to allow the rupture to expand or not during the initial interval of weak radiation. For the unilateral rupture model we use 21 subfaults along strike with 12 km lengths and 8 subfaults along dip with 4 km widths. The hypocenter is 12.5 km below sea level at 54.443°N, 168.857°E. The rupture expansion velocity is 2.15 km/s. The subfault source durations are parameterized with 10 2-s rise-time triangles, offset by 2-s each, permitting up to 22 s long subfault durations. For the bilateral rupture model we use 38 subfaults along strike with 12 km lengths and 8 subfaults along dip with 4 km widths. The hypocenter is 12.5 km below sea level at 54.593°N, 168.957°E. The rupture expansion velocity is 3.0 km/s. The subfault source durations are parameterized with 8 2-s rise-time triangles, offset by 2-s each, permitting up to 22 s long subfault durations.

Additional References

Fu, Y., & Freymueller, J. T. (2012). Seasonal and long-term vertical deformation in the Nepal Himalaya constrained by GPS and GRACE measurements. *J. Geophys. Res*., *117*, B03407, doi:10.1029/2011JB008925.

Zumberge, J. F., Heflin, M. B., Jefferson, D. C., Watkins, M. M., & Webb, F. H. (1997). Precise point positioning for the efficient and robust analysis of GPS data from large networks. *J. Geophys. Res., 102*(B3), 5005–5017, doi:10.1029/96JB03860.

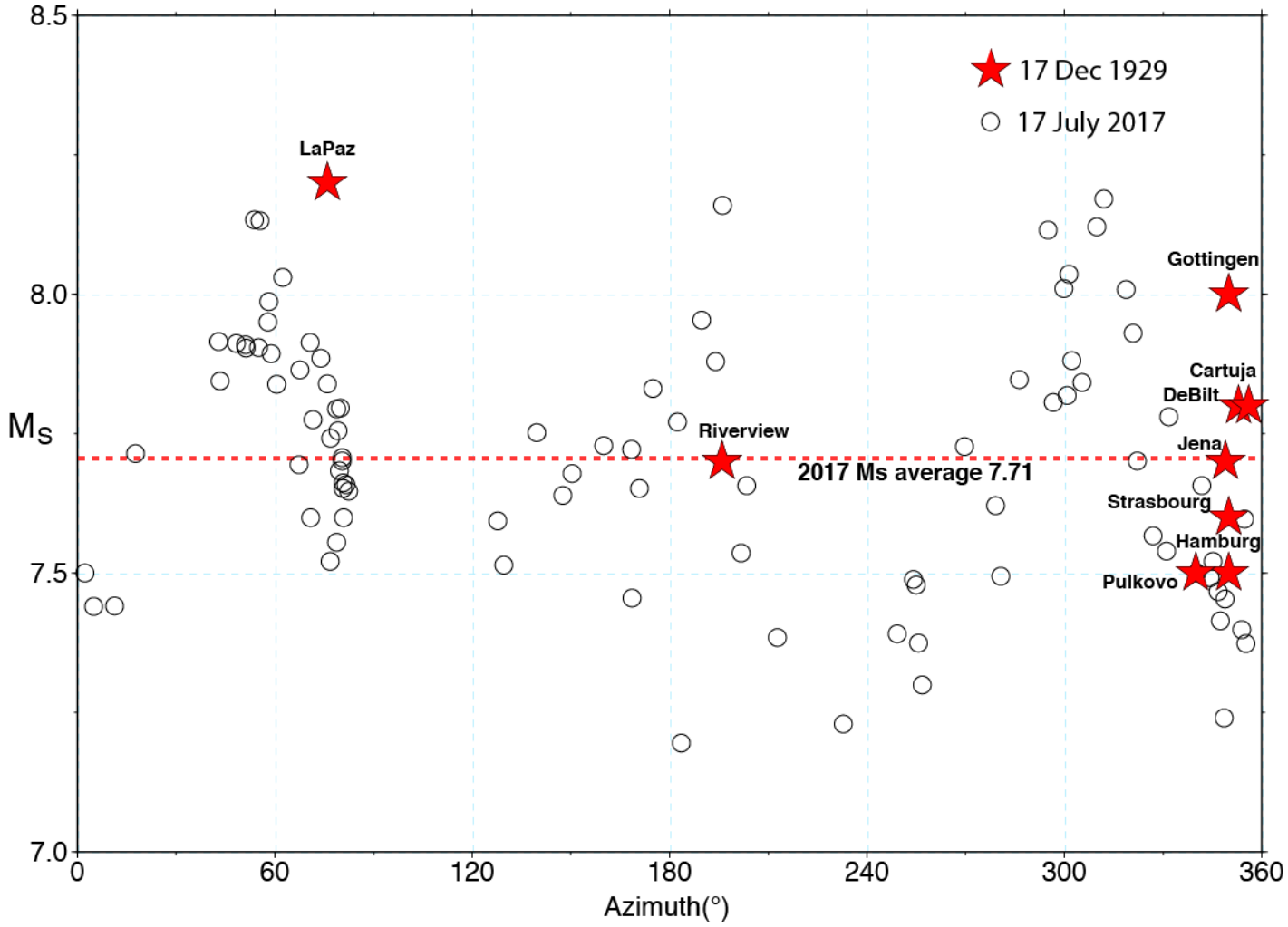

Figure S1. Measurements of M_S at stations with different azimuths for the 17 December 1929 Near Islands earthquake (red stars) and the 17 July 2017 Komandorsky Islands earthquake (open circles). Amplitude data for the 1929 event are from Gutenberg's notepad, and M_S values for the 2017 event are from the USGS/NEIC. Similar M_S at different azimuths suggests that two events are of comparable size.

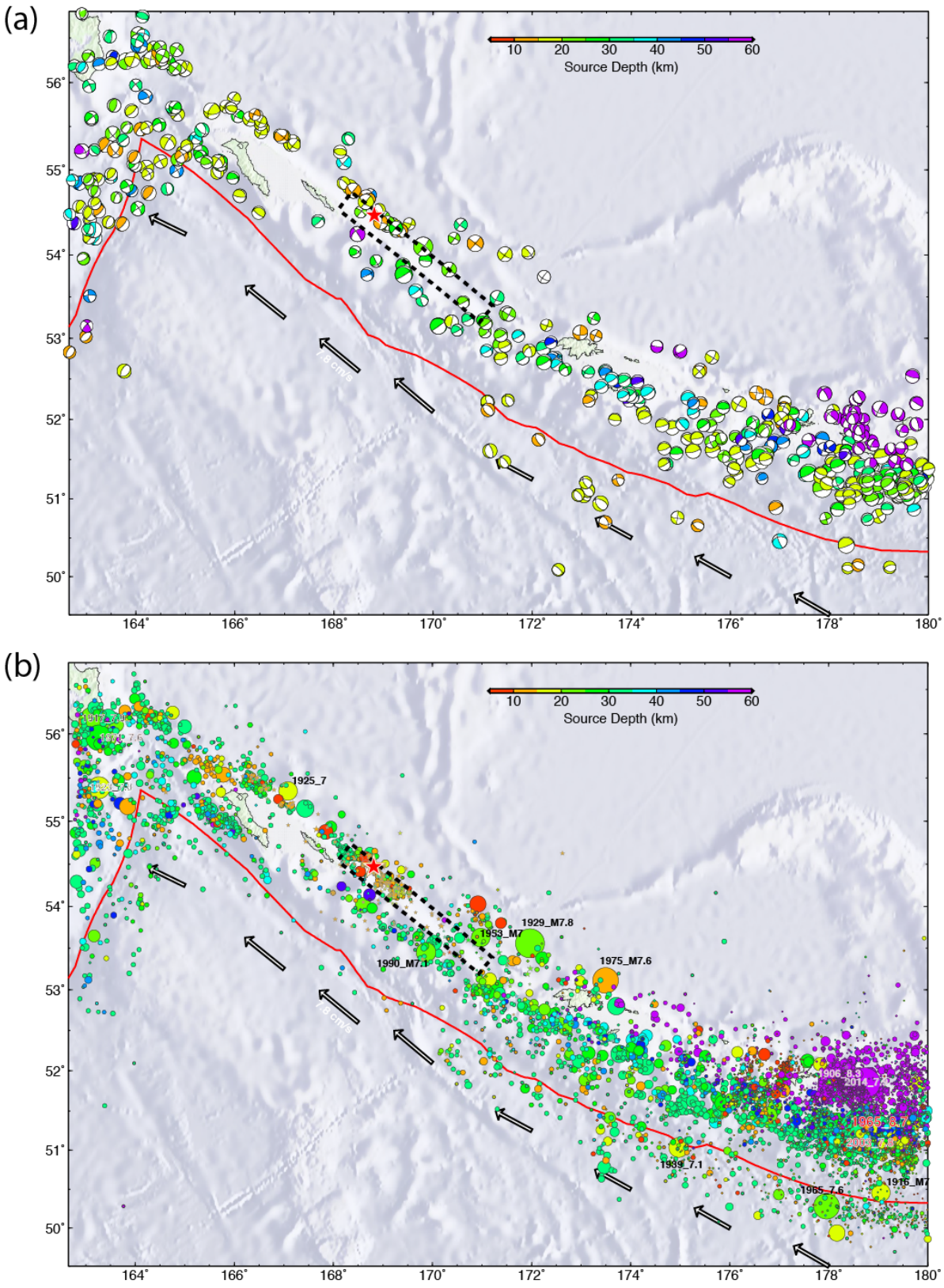

Figure S2. (a) Moment tensor solutions from the GCMT for the western Aleutians, color-coded by depth. (b) USGS-NEIC seismicity for the western Aleutians from 1900 to 2017, color-coded by depth.

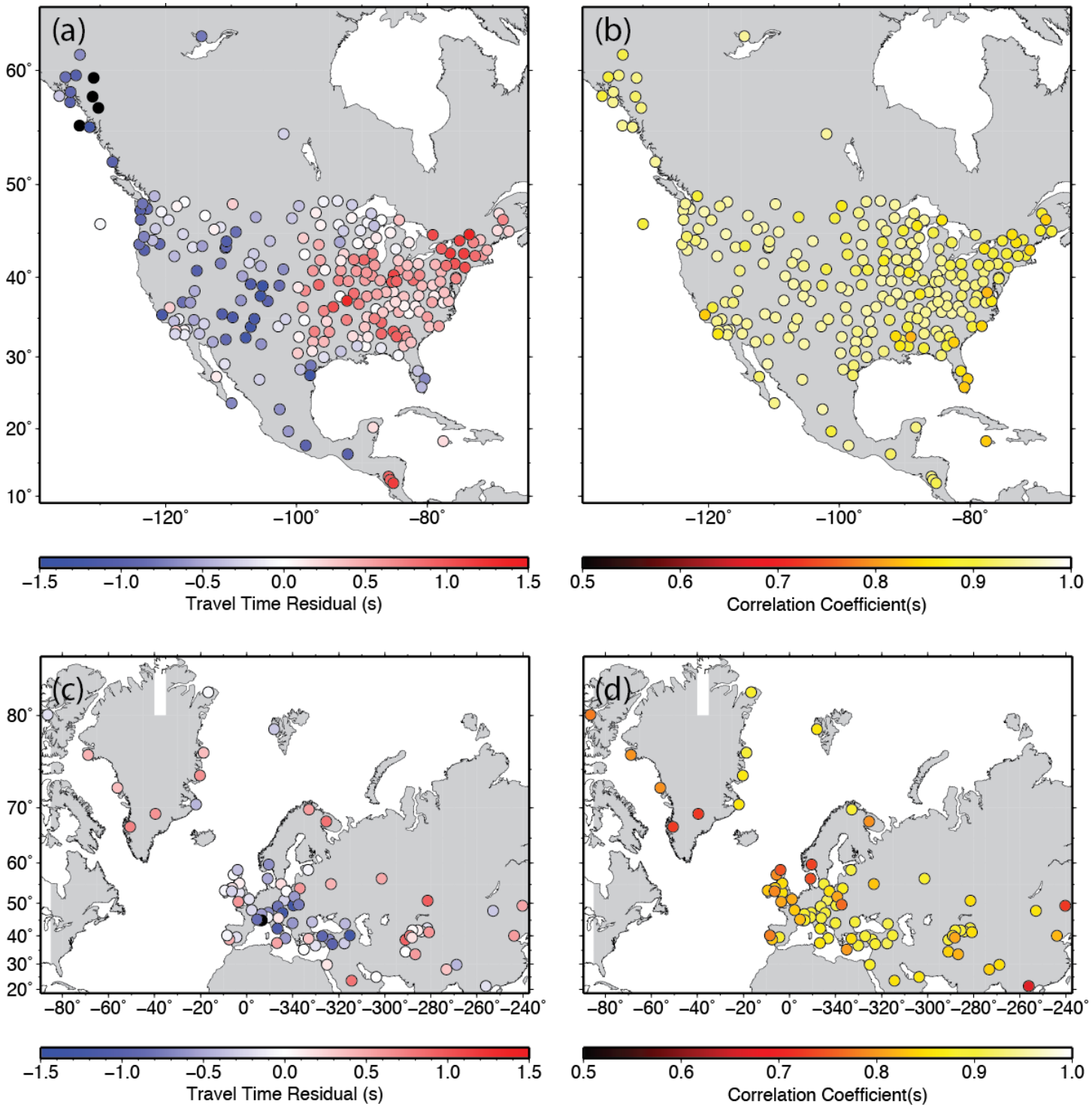

Figure S3. Station locations for large aperture arrays of broadband seismic stations for which filtered short-period *P* waves signals are used in back-projections for the 17 July 2017 earthquake rupture. (a) and (b) show the North American stations used with the time shifts from multi-station broadband correlations (a) and the correlation coefficients (b). (c) and (d) show the Eurasian and Greenland stations used with the time shifts from multi-station broadband correlations (c) and the correlation coefficients (d).

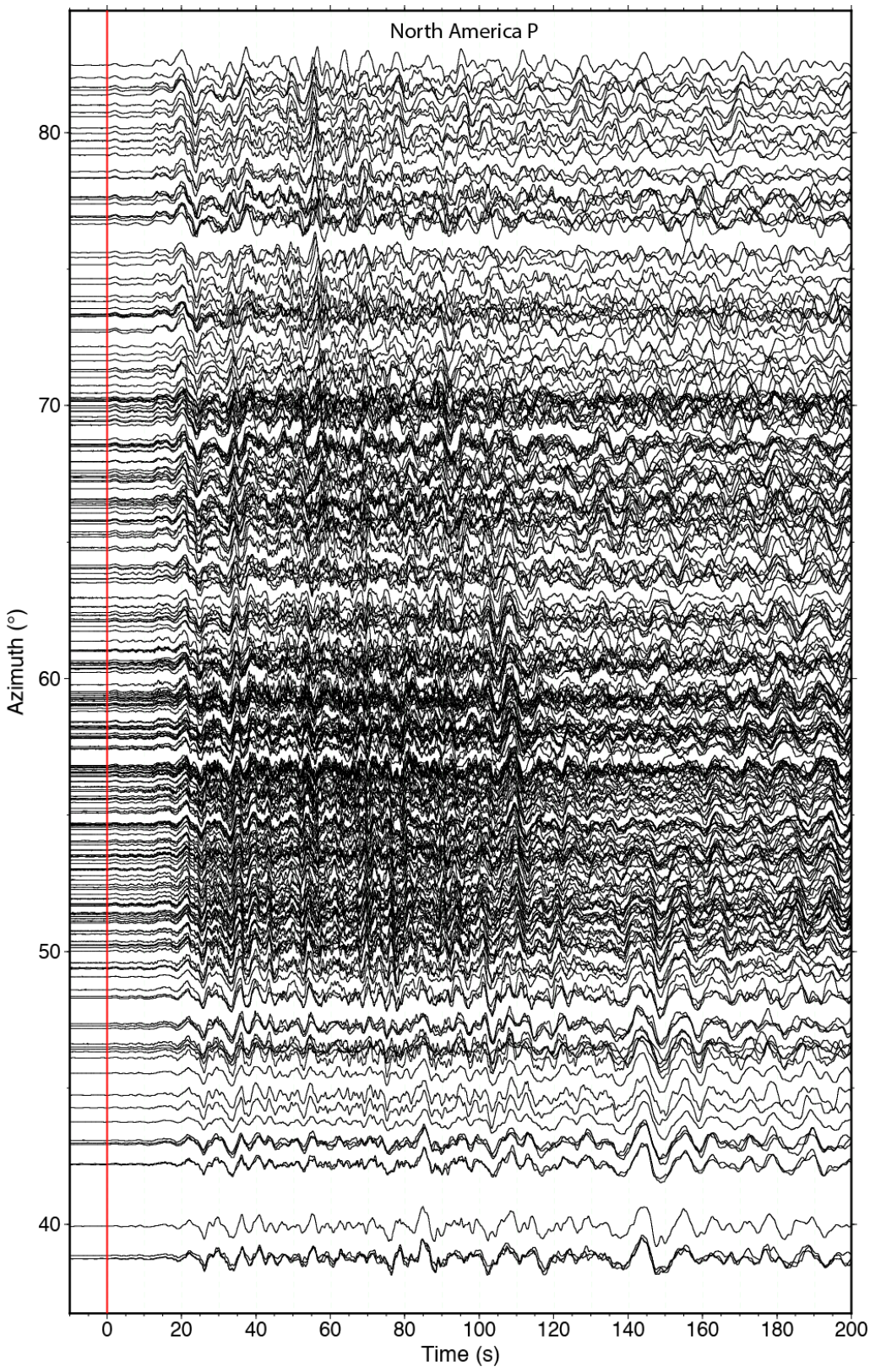

Figure S4. Azimuthal plot of the broadband *P* waves from North American stations in Figure S3a with time corrections applied. Note the ~15 s delay before strong arrivals.

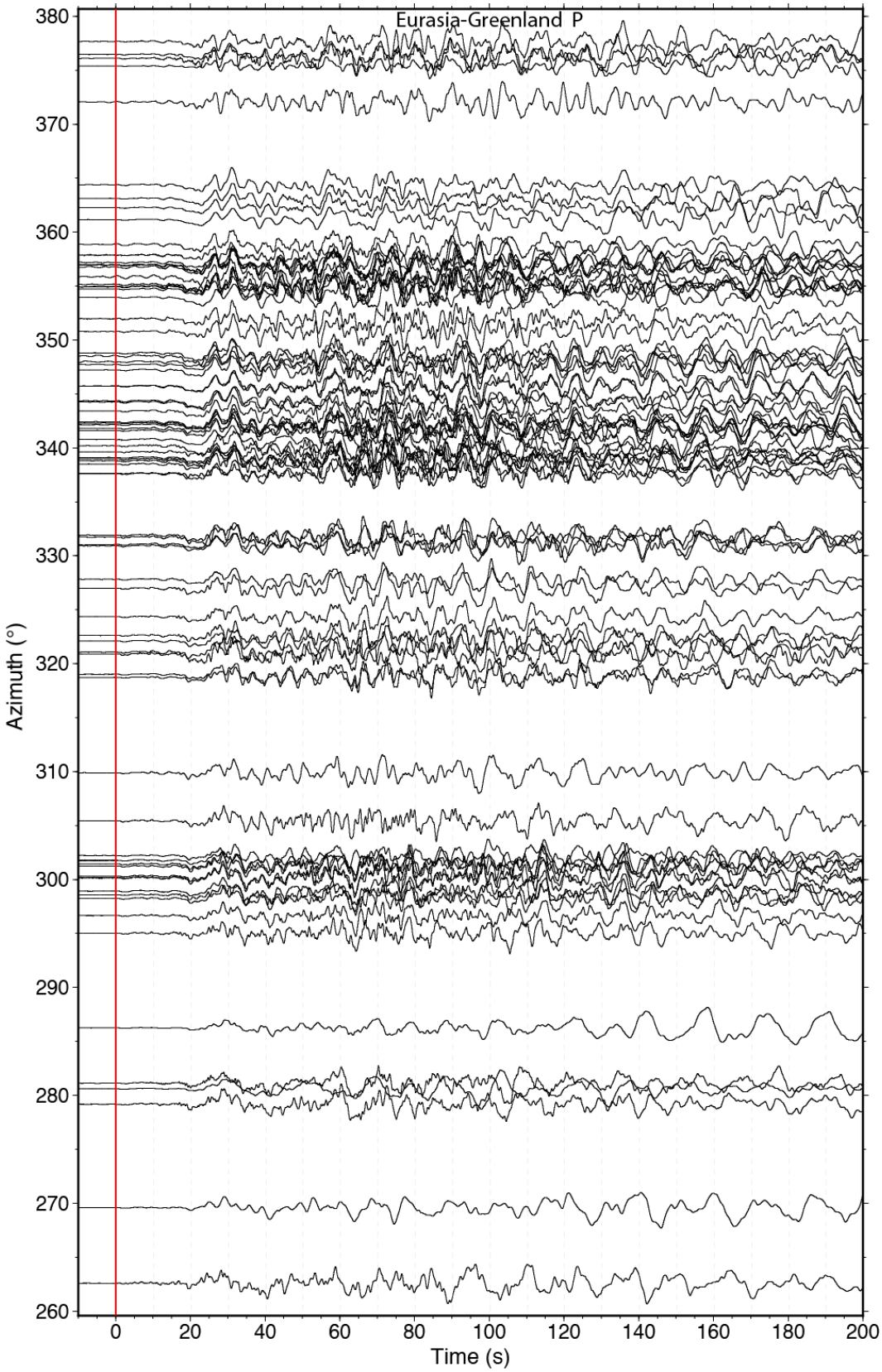

Figure S5. Azimuthal plot of the broadband *P* waves from Eurasian and Greenland stations in Figure S3c with time corrections applied. Note the ~15 s delay before strong arrivals.

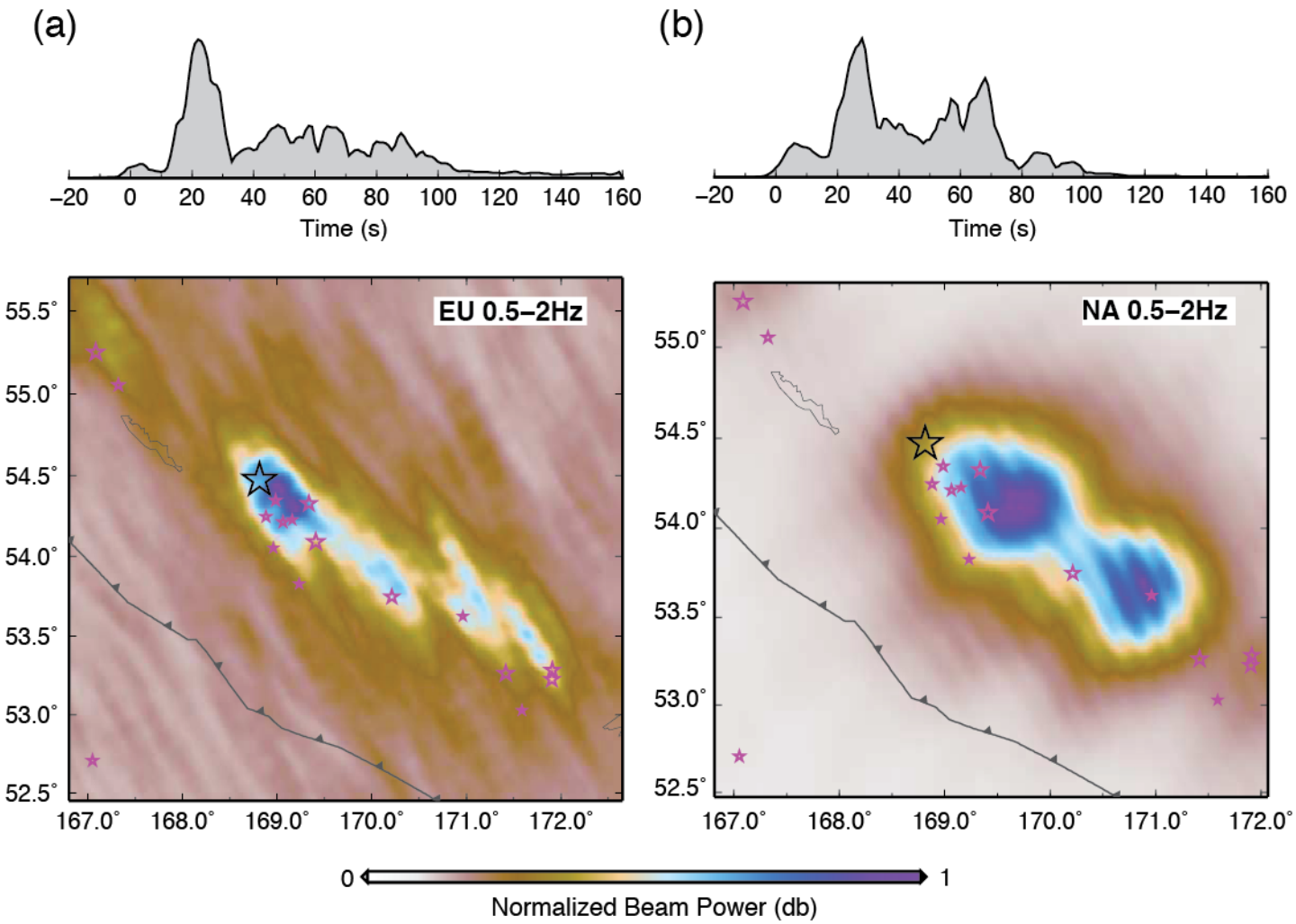

Figure S6. Time-integrated stacks of back-projection beam power for 0.5-2.0 Hz *P* waves for the signals from Eurasia and Greenland (a) and from North America (b). The fourth-root stacked beam power as a function of time for the two geometries is shown above each map. The black stars indicate the USGS/NEIC epicenter and the magenta stars are large aftershocks in the first day.

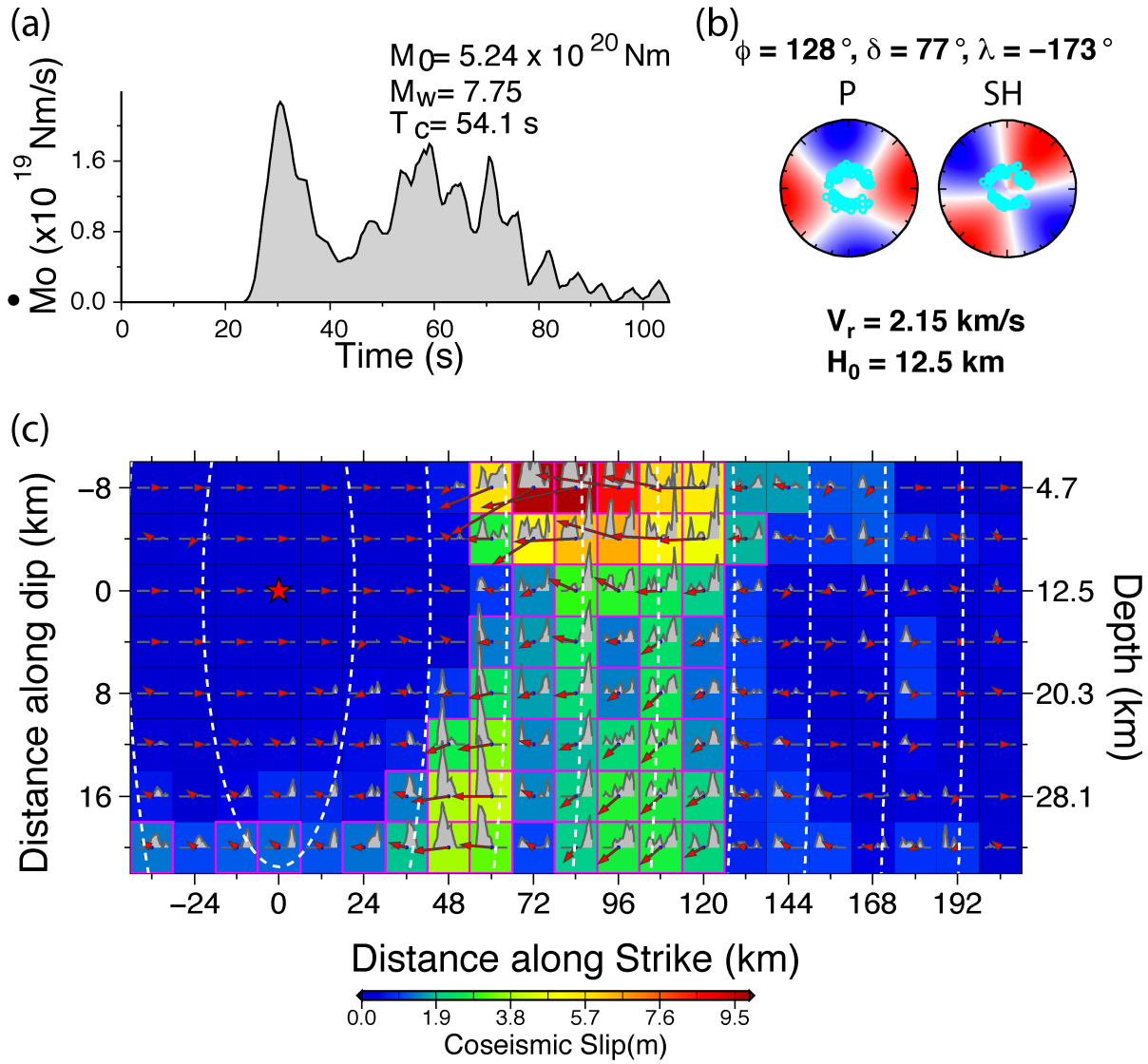

Figure S7. Unilateral finite-fault slip model for the 17 July 2017 Komandorsky Islands earthquake from inversion of teleseismic *P* and *SH* ground displacement waveforms. The moment rate function is shown in (a), with the seismic moment, M_0, M_W and centroid time, T_c being indicated. The average faulting geometry is shown in (b), along with the data distribution and radiation patterns for *P* and *SH* signals in lower hemisphere equal area projections. Red quadrants are compressional motions for *P* waves and clockwise rotation for *SH* waves. The rupture expansion velocity, V_r and hypocenter depth H_0 are shown. The slip distribution on the fault is shown in (c), as viewed from the southwest. Vectors indicate average slip and rake of the hanging wall (Komandorsky Sliver) relative to the footwall (Bering Plate). The color palette indicates the slip magnitude for each subfault. The subfault moment rate functions are shown by the polygons inside each slip, with total durations of up to 22 s. Isochrones of rupture front location in 10 s intervals are indicated by white dashes. The hypocenter is indicated by the red star.

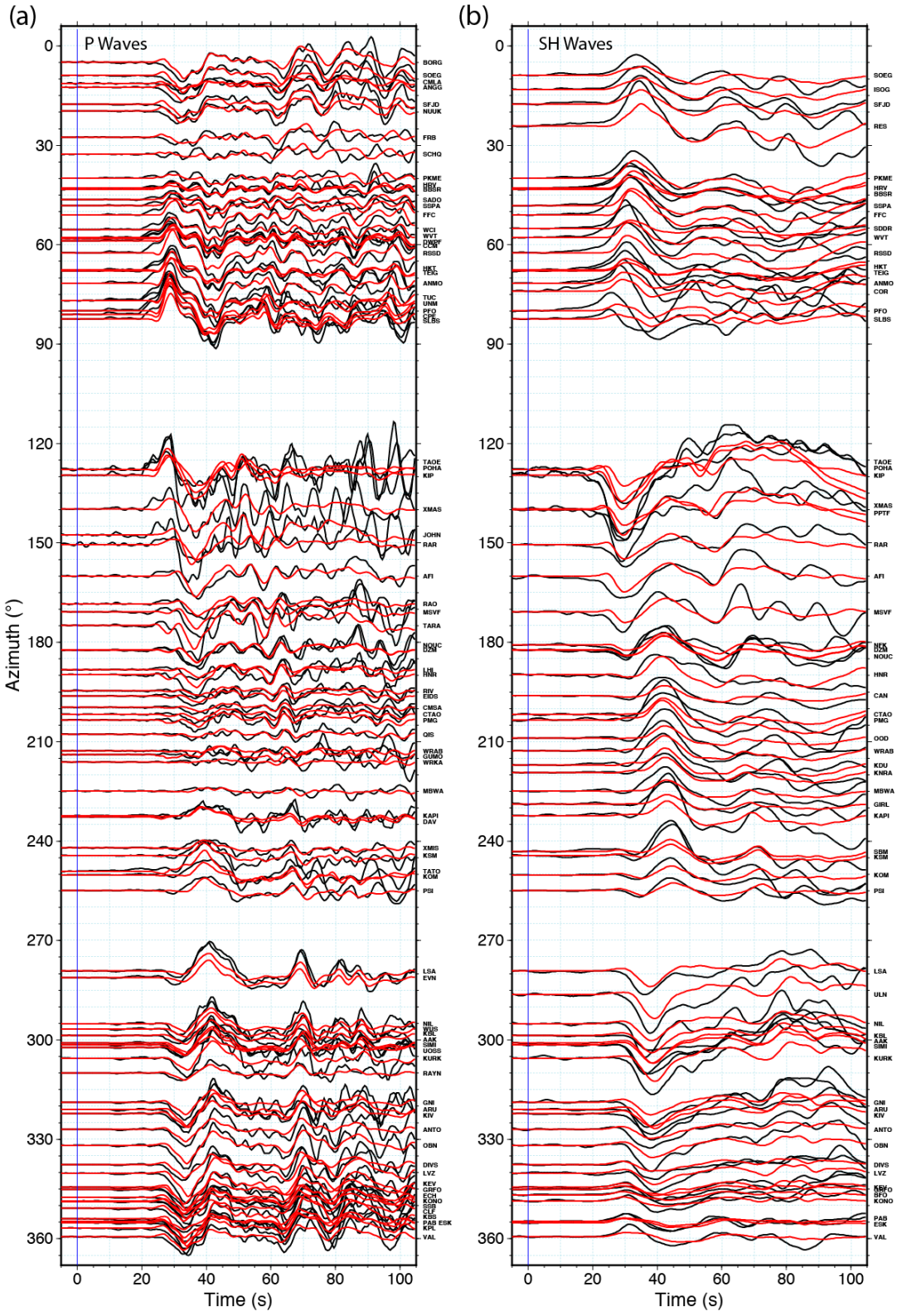

Figure S8. Azimuthal distributions of (a) *P* wave observations (black curves) and synthetics (red curves) for the unilateral fault model in Figure S7, and (b) *SH* wave observations (black curves) and synthetics (red curves).

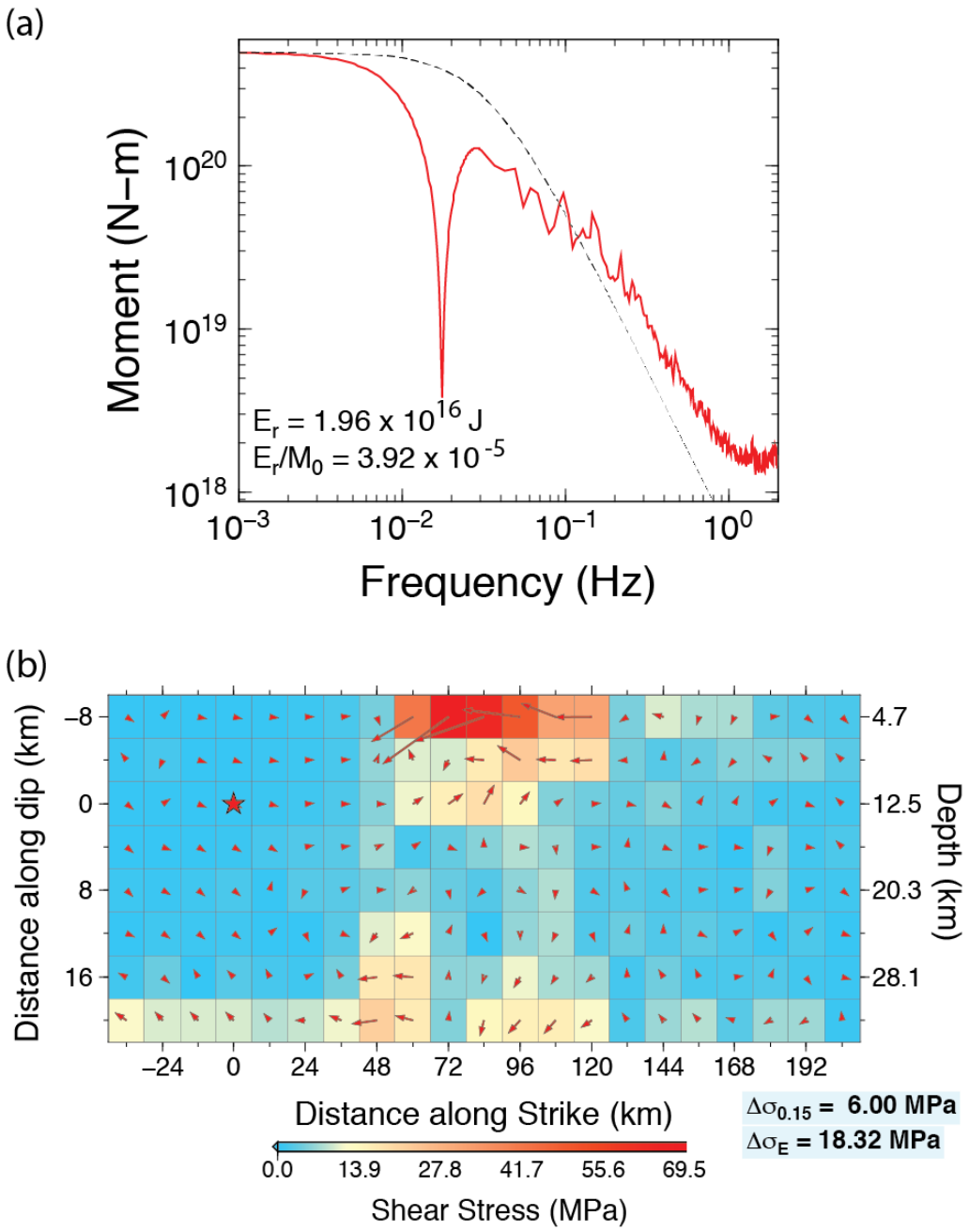

Figure S9. (a) Far-field source spectrum for the unilateral model (Figure S7) obtained by combining the spectrum of the moment rate function for frequencies less than 0.05 Hz with the logarithmic average of globally distributed *P* wave spectra for frequencies higher than 0.05 Hz. The dotted line is a reference ω-squared spectrum with corresponding seismic moment and a stress factor of 3 MPa. The broadband radiated seismic energy, E_r, estimated from the teleseismic *P* wave observations using the method of Ye et al. (2016), and the seismic moment-scaled value are shown. (b) Static shear stress for the unilateral slip model for the 17 July 2017 Komandorsky Islands earthquake with the magnitude and direction for each subfault being shown. The average static shear stress drop for the model is 6 MPa using a procedure that removes all subfaults with seismic moment less than 15% of the peak subfault seismic moment. The slip-weighted average stress drop obtained using the method of Ye et al. (2016) gives a higher value of 18 MPa.

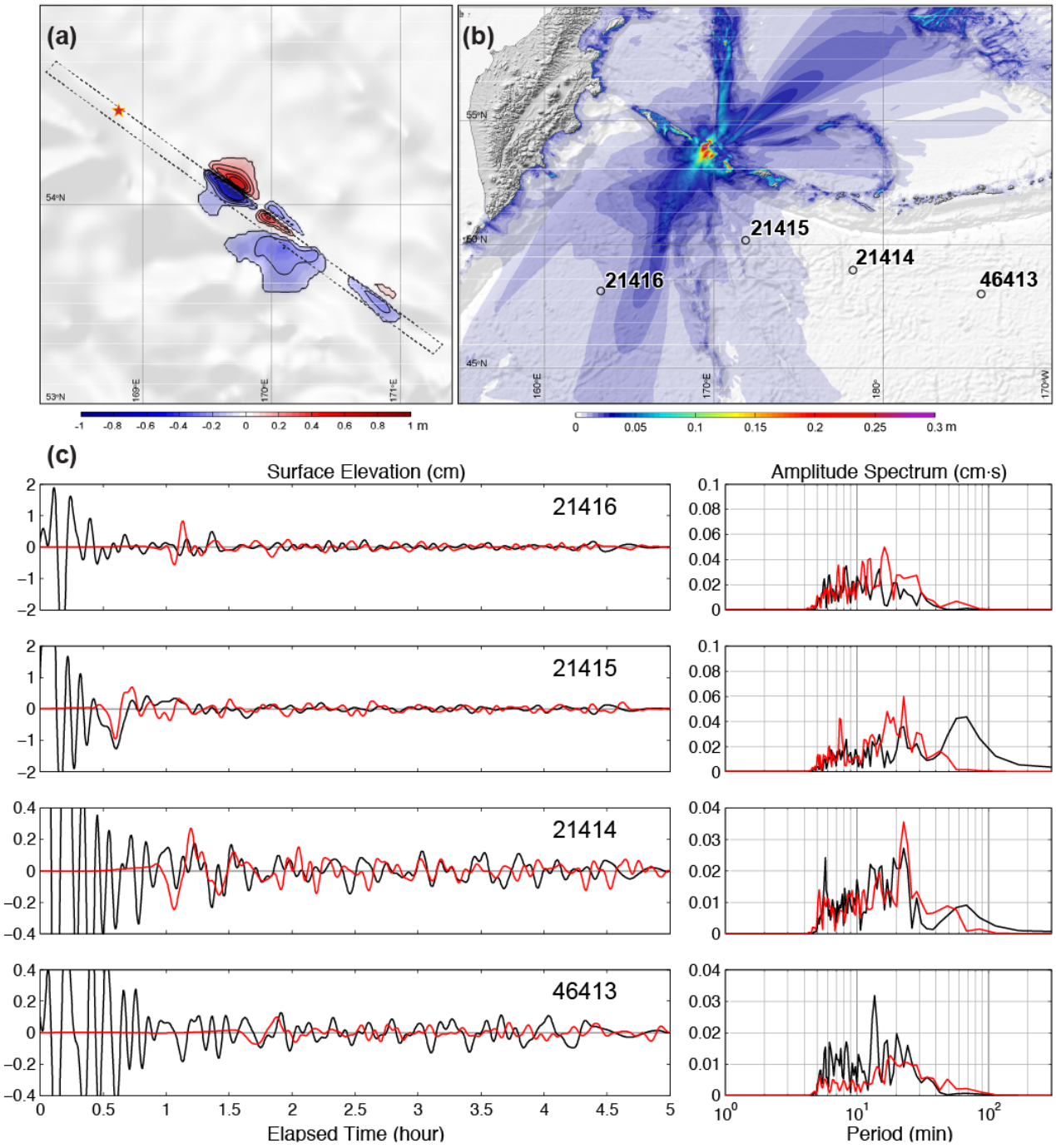

Figure S10. Predicted tsunami from the unilateral faulting model. (a) Final seafloor deformation with the red star indicating the epicenter and the dash line delineating projection of the faulting model on the seafloor. (b) Predicted tsunami amplitude and DART stations (circles) considered in this study. (c) Comparison of filtered sea surface recordings (black traces) at DART stations with predictions (red). The recorded and predicted time series were filtered to remove signals shorter than 5 min period and the full 5-hr time series were used in the computation of the amplitude spectra. The strike-slip faulting and position of the stations results in weak tsunami waves, but the timing and height of long-period arrivals provide bounds on the source.

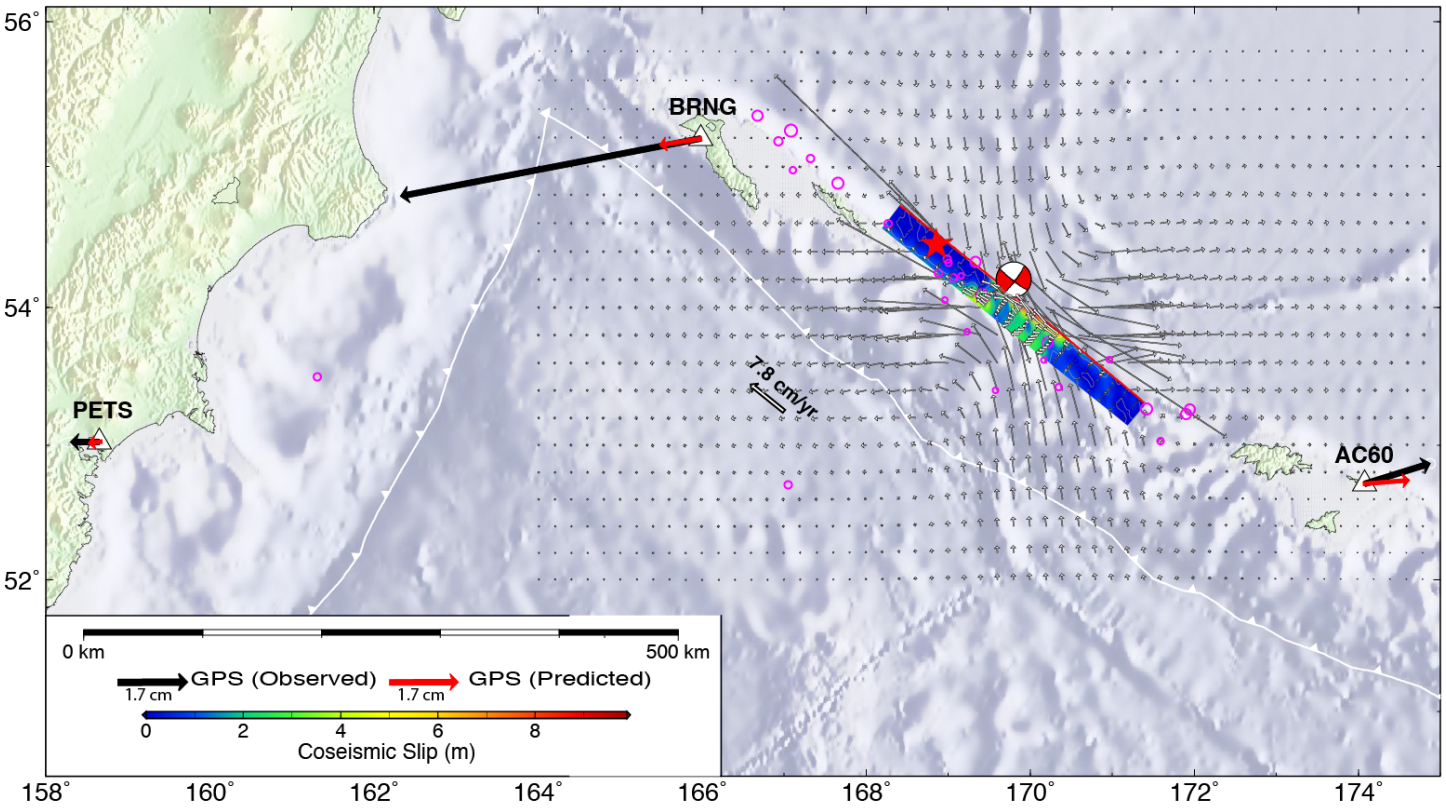

Figure S11. Prediction of GPS horizontal motions at stations BRNG (Bering Island), AC60 and PETS for the unilateral slip model. The observed GPS deformations are black arrows, the predicted values at those locations are red arrows. The grid of vectors indicates the spatial variation of predicted horizontal surface motions on 1/20th scale. The unilateral slip model location is shown in the rectangle, with early aftershock locations indicated by magenta circles and the *W*-phase moment tensor solution shown by the red focal mechanism.

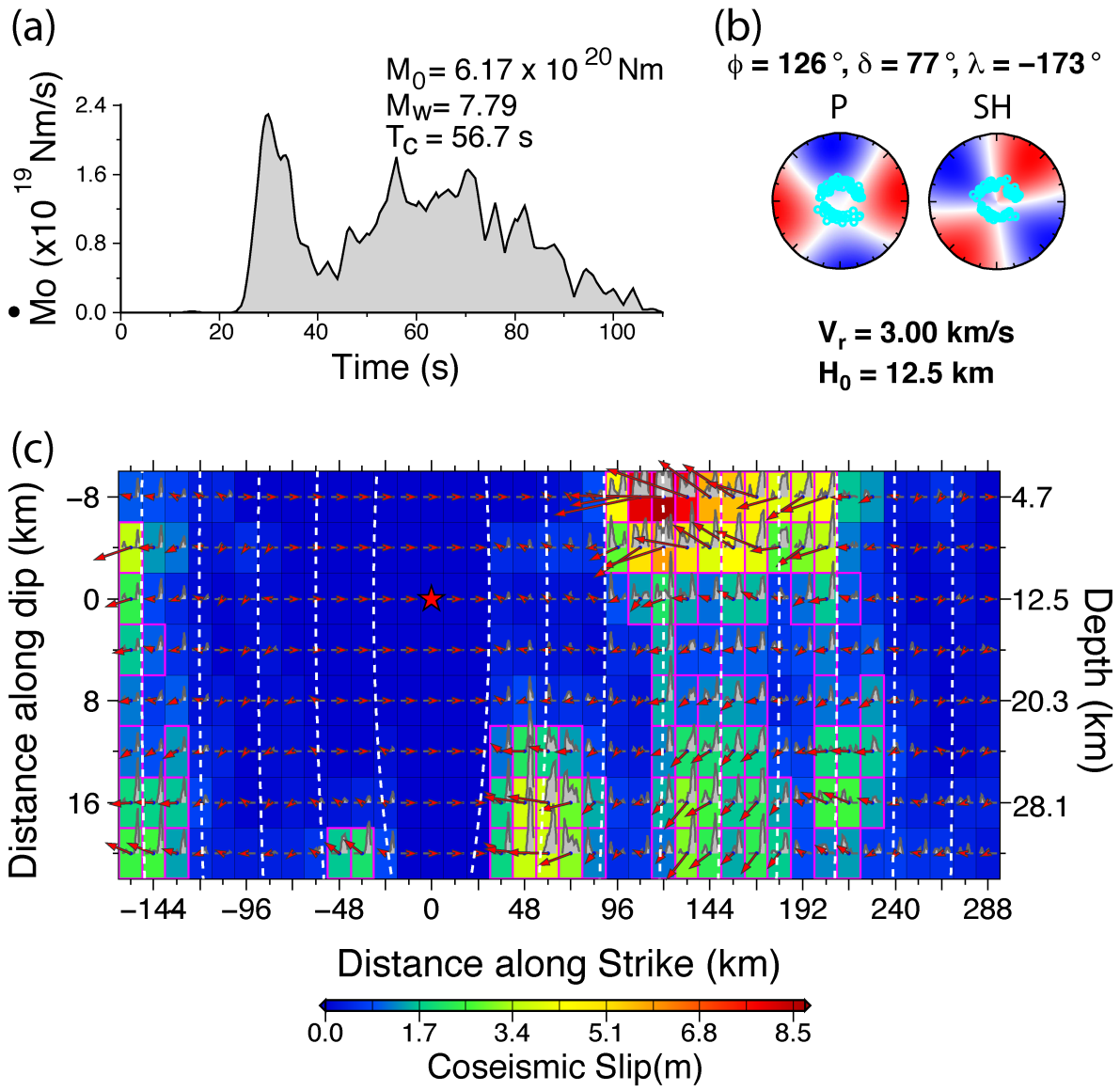

Figure S12. Preferred bilateral finite-fault slip model for the 17 July 2017 Komandorsky Islands earthquake from inversion of teleseismic *P* and *SH* waveforms. The moment rate function is shown in (a), with the seismic moment, M_0, M_W and centroid time, T_c being indicated. The average faulting geometry is given in (b), along with the data distribution and radiation patterns for *P* and *SH* signals in lower hemisphere equal area projections. Red quadrants are compressional motions for *P* waves and clockwise rotation for *SH* waves. The rupture expansion velocity, V_r and hypocenter depth H_0 are shown. The slip distribution on the fault is shown in (c), as viewed from the southwest. Vectors indicate average slip and rake of the hanging wall (Komandorsky Sliver) relative to the footwall (Bering Plate). The color palette indicates the slip magnitude for each subfault. The subfault moment rate functions are shown by the polygons inside each slip, with total durations of up to 18 s. Isochrones of rupture front location in 10 s intervals are indicated by white dashes. The hypocenter is indicated by the red star. The model is shown in map view in Figures 2 and 4.

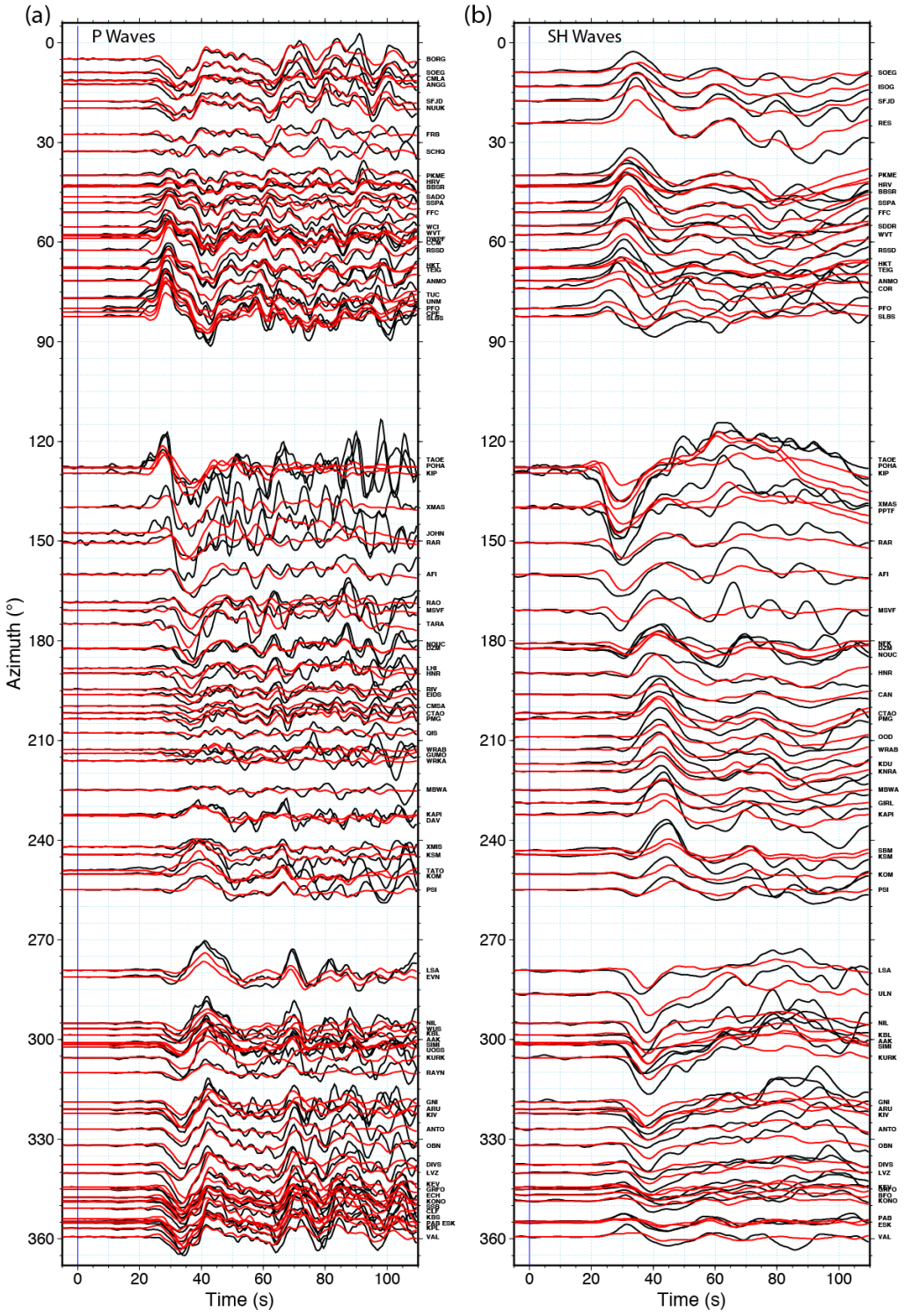

Figure S13. Azimuthal distributions of (a) *P* wave observations (black curves) and synthetics (red curves) for the preferred bilateral fault model (Figures 2, 4, S12), and (b) *SH* wave observations (black curves) and synthetics (red curves).

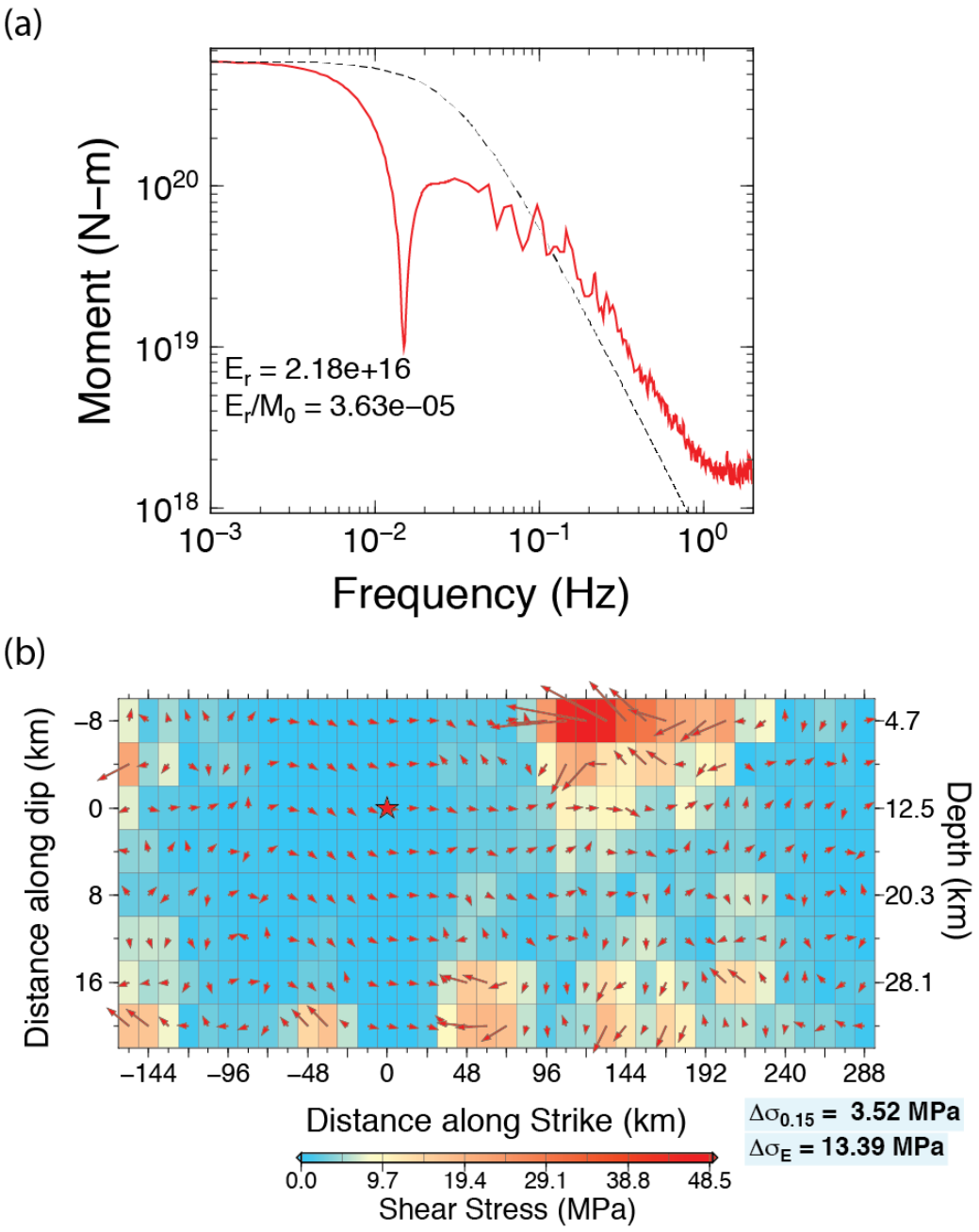

Figure S14. (a) Far-field source spectrum for the preferred bilateral model (Figures 2, 4, S12) obtained by combining the spectrum of the moment rate function for frequencies less than 0.05 Hz with the logarithmic average of globally distributed *P* wave spectra for frequencies higher than 0.05 Hz. The dotted line is a reference ω-squared spectrum with corresponding seismic moment and a stress factor of 3 MPa. The broadband radiated seismic energy, E_r, estimated from the teleseismic *P* wave observations using the method of Ye et al. (2016), and the seismic moment-scaled value are shown. (b) Static shear stress for the unilateral slip model for the 17 July 2017 Komandorsky Islands earthquake with the magnitude and direction for each subfault being shown. The average static shear stress drop for the model is 3.5 MPa using a procedure that removes all subfaults with seismic moment less than 15% of the peak subfault seismic moment. The slip-weighted average stress drop obtained using the method of Ye et al. (2016) gives a higher value of 13.4 MPa.

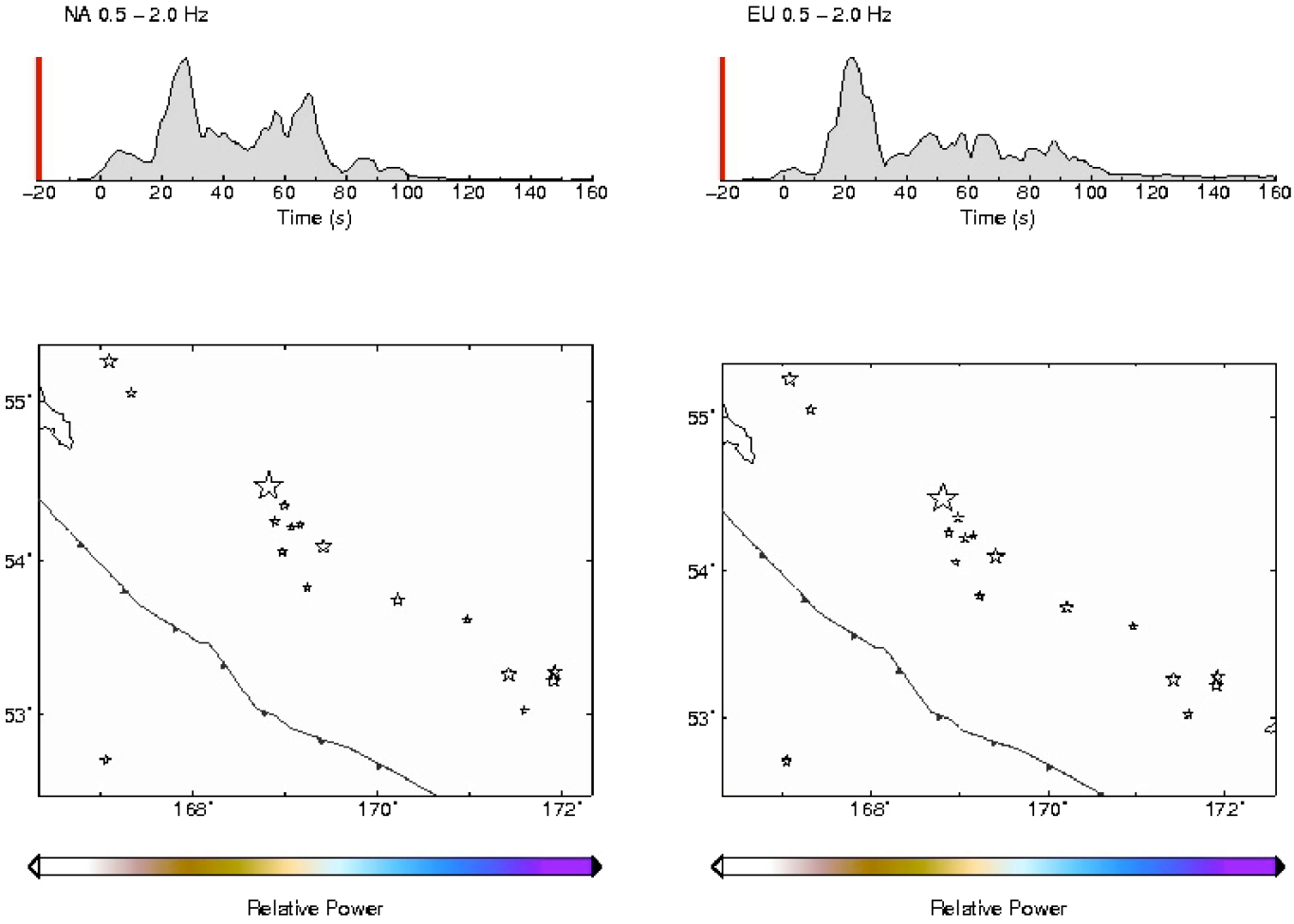

Animation A1. Back-projection of 0.5-2.0 Hz *P* wave data from the large aperture networks in North America (left) and Eurasia-Greenland (right) (see Figure S3). The fourth-root beam power is shown around the source region. The large star is the 17 July 2017 mainshock epicenter. Smaller stars are aftershocks in the first day.